The Thesis Committee for Sean Andrew Lanham
certifies that this is the approved version of the following thesis:

Quantum Information Processing Approaches in Classical Systems

SUPERVISING COMMITTEE:

Robert W. Heath Jr., Supervisor

Brian R. La Cour

Quantum Information Processing Approaches in Classical Systems

by

Sean Andrew Lanham

THESIS

Presented to the Faculty of the Graduate School of

The University of Texas at Austin

in Partial Fulfillment

of the Requirements

for the Degree of

MASTER OF SCIENCE IN ENGINEERING

THE UNIVERSITY OF TEXAS AT AUSTIN

August 2019

Acknowledgments

I'm very grateful to both members of my thesis committee for their exceptional support and guidance through my degree process. I'd like to express thanks to Dr. Brian La Cour for leading me to exciting areas of research and always being available to challenge me and sharpen my arguments. I'd like to thank Dr. Robert W. Heath Jr. for his valuable research insights and enthusiasm to investigate interesting problems at the intersection of quantum computing and signal processing. There is no doubt that both will continue to inspire my development as a researcher, technical writer, and engineer.

I'd also like to acknowledge and thank everyone at the Applied Research Laboratories Center for Quantum Research and the role they played in this research, especially Dr. Granville Ott for his seemingly unrivaled expertise in analog circuits. The atmosphere of collaboration and cross-disciplinary discussion at the Center has been invaluable in conducting this research.

Finally, I'd like to thank all my family and friends for their love and support during these years, especially those who were with me throughout the entire journey. I'm very grateful to my parents Carol and Sean Lanham, my brother Michael Lanham, aunts and uncles who always encouraged my academic endeavors, and close friends like Ginger Huh for their support.

Quantum Information Processing Approaches in Classical Systems

Sean Andrew Lanham, M.S.E.
The University of Texas at Austin, 2019

Supervisor: Robert W. Heath Jr.

The engineering problem of building scalable quantum computers has prompted the development of a rich theory modeling the evolution of quantum systems as well as techniques to preserve quantum information in the presence of noise. Such techniques offer systems-level approaches to the problem of robustly encoding and preserving information and, as a result, see applicability in a wide variety of architectures for computing systems. In this thesis, we visit the mathematical underpinnings of quantum information and apply strategies inspired by quantum information processing to two non-quantum systems to demonstrate advantage. We first describe the construction of a *quantum emulation device*, an analog electronic system with the same mathematical structure as a gate-based quantum computer, and introduce novel time-domain information encoding methods to increase the computational capacity of the device. We confirm the sustained performance of the improved system by successfully transforming emulated states by randomly selected quantum gates.

We then visit similarities between quantum information processing and signal processing in the noncoherent wireless communication setting, the latter being an environment characterized by a lack of instantaneous channel knowledge. We describe the theoretical underpinnings of the noncoherent communication environment from both an information theoretic and signal processing perspective. This leads us to propose a multi-antenna space-time code construction based on a family of quantum error correcting codes known as stabilizer codes. For this code, we derive the optimal decoder in Rayleigh and Ricean fading and benchmark the its performance against coherent and differential coding at comparable rates.

Table of Contents

List of Tables

List of Figures

Chapter 1

Introduction

Quantum computers are expected to exhibit computational speedups compared to digital processors by leveraging advantageous properties of quantum systems. For example, using the property of linear state superposition, a maximum of 2^n binary states can be represented and processed simultaneously using an n-qubit quantum system. This gives rise to a notion of "quantum parallelism," which is exploited to reduce the number of manipulations required to arrive at a solution [17]. Using these ideas, quantum algorithms have been proposed to tackle problems believed to be computationally hard, such as factoring [79] and unstructured search problems [25], demonstrating lower computational complexity than standard approaches with digital computers.

Quantum systems also behave in ways that confound attempts to apply standard information processing methods. For example, another important property of quantum systems is that outside interaction with the system arising from a measurement or observation causes its state to change. Because of this, the state of a quantum system is never known with certainty, and approaches to processing quantum information cannot assume explicit access to this infor-

mation. From an engineering vantage point, this feature of quantum systems typically places limitations on possible processing and information preservation methods, requiring new approaches to address these issues. The theory of quantum error correction, for example, provides many ingenious methods for recovering quantum information with only statistical knowledge of the state of a noisy system or the noisy channel that corrupted it.

Current approaches to quantum computing rely on the careful manipulation of quantum physical systems. Examples include photonic computing systems [70], trapped ion systems [30], and superconducting systems [77]. The state preparation and manipulation required to perform reliable computational processing with such systems remains a daunting engineering task. They are extremely sensitive to the effects of noise arising from small interactions with the external environment. These degrading effects gradually accumulate, leading to a process known as *decoherence*, which typically corresponds to a loss of quantum information [62]. This issue is further compounded by the "no-cloning" theorem, which states that an identical copy of a quantum system cannot be reliably constructed, preventing information preservation through redundancy.

Interestingly, the mathematical framework underpinning a quantum system can be found, or engineered, in systems behaving according to classical physics. Gate-based quantum computers, in particular, possess a Hilbert space mathematical structure similar to some non-quantum, or classical, systems [47,80]. Motivated by this insight, we focus on analyzing classical systems

with the aim of identifying advantages similar to those presented by true quantum information processing systems. We present extensions of an information encoding approach for an analog electronic system termed a *quantum emulation device*, first presented in [47]. In this classical system, properties such as linear superposition are still exhibited, while the overall robustness to noise of the system improves with respect to important metrics when compared to true quantum computing systems. Our new encoding method extends on previously developed frequency-domain encoding methods, allowing emulated qubits to be encoded in the time-domain and significantly increasing the computational capacity of a device with minimal impact to overall performance. These results are confirmed with a prototype implementation of the device.

Additionally, we focus on a mathematical similarity between the situation of preserving quantum information traveling through a channel, during which the state of both the system and the channel cannot be exactly determined, and a wireless cellular noncoherent communication system, which is characterized by a lack of instantaneous channel knowledge at both the transmitter and receiver. In the classical setting, we adapt a quantum error correcting code, designed to preserve quantum information without requiring state or channel knowledge, to the wireless setting, modifying the design to make use of the additional information afforded in the non-quantum regime. The result is a space-time code designed for the noncoherent multi-antenna communication setting. We construct the codebook taking into account insights from noncoherent communication signal processing and information theory.

The thesis is organized as follows. Section 2 introduces concepts from quantum information that are important for understanding the design of our classical systems. We focus particularly on a class of quantum error correcting codes known as stabilizer codes, since they feature prominently in later sections. In Section 3 we detail the mathematical framework of the quantum emulation device, presenting a time-domain emulated qubit encoding method termed *time-bin encoding*. We also detail an implementation of the device on a printed circuit board and characterize its processing performance for time-bin qubits. In Section 4 we motivate the introduction of a novel multi-antenna space-time code by summarizing the existing results on the noncoherent capacity of a communication channel in more detail, focusing on results for fast-fading and at finite blocklength. In Section 5 we review noncoherent signaling approaches based on those capacity results, integrating important signal processing considerations such as receiver complexity, power efficiency, and codebook design. Finally, in Section 6 we fully describe the requisite ideas that lead to the design of a noncoherent space-time code based on a quantum error correcting code. We describe the maximum likelihood decoder for the Rayleigh and Ricean fading setting and provide simulations for the code's performance against comparable coherent and noncoherent approaches in Rayleigh fading.

The following notation is used in this paper. We use bold lower case letters $\mathbf{a}$ to denote column vectors, and bold upper case letters $\mathbf{A}$ to denote matrices. We use non-bold letters to denote scalars. We denote the element in

the i^{th} row and k^{th} column of a matrix $\mathbf{A}$ by $[\mathbf{A}]_{i,k}$. In general we denote the $k \times k$ identity matrix by $\mathbf{I}_k$. The 2×2 identity matrix is used so often that we drop the subscript, i.e. $\mathbf{I}_2 = \mathbf{I}$. We use $\text{tr}(\mathbf{A})$ to denote the trace, $\det(\mathbf{A})$ the determinant, $\mathbf{A}^T$ the transpose, and $\mathbf{A}^*$ the conjugate transpose. For positive semi-definite matrices, $\mathbf{A}^{\frac{1}{2}}$ denotes the matrix square root. We use $|a|$ to denote the absolute value of a scalar. We use $\mathbb{E}(\cdot)$ to denote expectation. We use $\otimes$ to denote the tensor product when acting on vector spaces (i.e. $\mathbb{C}^2 \otimes \mathbb{C}^2$) and to denote the Kronecker product when acting on vectors or matrices. We use $\mathcal{N}_C(\boldsymbol{\mu}, \boldsymbol{\Sigma})$ to denote a complex circularly symmetric normal distribution with mean $\boldsymbol{\mu}$ and covariance $\boldsymbol{\Sigma}$. If $A = cB$ where $c > 0$, we write $A \propto B$. The indicator function of a subset $[a, b]$ of the real numbers is denoted $\mathbb{1}[a, b](x)$. Function composition is represented using $\circ$, where $f \circ g(x) = f(g(x))$. The vector space of complex valued square integrable functions defined on the interval $[a, b]$ is $L^2[a, b]$.

Chapter 2

Review of Quantum Information

In this chapter we review some material from quantum information processing. We begin by introducing general systems of *qubits*, or quantum bits, that are the natural generalization of a bit in quantum computing. We continue with a definition of an important measure of distance between quantum states. We then turn to quantum gates, the fundamental objects used to manipulate quantum systems. Finally, we describe stabilizer codes, a powerful class of quantum error correcting codes which will feature in our space-time code construction in Section 6.

2.1 Quantum States, Measurements, and Fidelity

A qubit represents the state of a two-level quantum system, such as the polarization of a photon, and is the most elementary example of quantum state. A qubit is represented as a state vector $\mathbf{q} = [\alpha, \beta]^T \in \mathbb{C}^2$ with

$$\mathbf{q}^*\mathbf{q} = |\alpha|^2 + |\beta|^2 = 1 \tag{2.1}$$

Portions of this review appeared in Lanham, S. Andrew, et al. "A Noncoherent Space-Time Code from Quantum Error Correction." 2019 53rd Annual Conference on Information Sciences and Systems (CISS). IEEE, 2019. Authors contributed equally.

by convention. Equipping $\mathbb{C}^2$ with the standard inner product $\langle \mathbf{q}, \mathbf{p} \rangle = \mathbf{q}^* \mathbf{p}$ leads us to define a qubit state as an element of a two-dimensional complex Hilbert space. In discrete time, the evolution of a closed quantum system is unitary. That is to say, $\mathbf{q}_{n+1} = \mathbf{U}\mathbf{q}_n$, where $\mathbf{U} \in \mathbb{C}^{2\times 2}$ with $\mathbf{U}^*\mathbf{U} = \mathbf{I}$. The concept of *applying* unitary operators (which is possible to good approximation) comes up often in quantum computing and will be used in this paper [62].

In general, the act of measuring, or observing, a quantum state causes the system to change. An important class of quantum measurements are *projective measurements*. Projective measurements are defined in terms of an *observable*, a Hermitian operator $\mathbf{M}$ on of the system of interest [62]. Let m denote an eigenvalue of $\mathbf{M}$ and let $\mathbf{P}_m$ be the projector onto the m eigenspace. The observable $\mathbf{M}$ can thus be orthogonally diagonalized as

$$\mathbf{M} = \sum_m m\mathbf{P}_m \ , \tag{2.2}$$

where $\mathbf{P}_n\mathbf{P}_m = \mathbf{0}$ when $n \neq m$. The outcome of "measuring the observable $\mathbf{M}$" is an eigenvalue m. If $\boldsymbol{\psi}$ is a quantum state, then the probability of measuring m is given by $p(m) = \boldsymbol{\psi}^*\mathbf{P}_m\boldsymbol{\psi}$ [62]. Given that the outcome m occurs, the system after measurement collapses to the state $\mathbf{P}_m\boldsymbol{\psi}/\sqrt{p(m)}$ [62]. It turns out that projective measurements, coupled with unitary evolution, fully describe general quantum measurements [62].

A notable feature of quantum measurement is that the *global phase* of a state is not observable. If $\mathbf{x} = [\alpha, \beta]^T$ and $\mathbf{y} = e^{j\theta}[\alpha, \beta]^T$, then, for a measurement in all possible bases, the distributions of outcomes for $\mathbf{x}$ and $\mathbf{y}$ are

the same. For this reason, one often works with *density matrices*. A state $\mathbf{q}$ can be represented by its density matrix $\mathbf{Q} = \mathbf{q}\mathbf{q}^*$. All of our previous formalism can be represented analogously. A state $\mathbf{Q}$ that evolves by the unitary $\mathbf{U}$ becomes the state $\mathbf{U}\mathbf{Q}\mathbf{U}^*$. The Born rule for projective measurements says that a state $\mathbf{Q}$ evolves to $\mathbf{P}_m\mathbf{Q}\mathbf{P}_m/p(m)$ with probability $p(m) = \mathrm{Tr}(\mathbf{P}_m\mathbf{Q}\mathbf{P}_m)$. Density matrices additionally provide a convenient way to describe quantum systems that have classical uncertainty. If a system is prepared in the state $\boldsymbol{\psi}_i$ with probability p_i, then the system is represented by the density matrix [62]

$$\mathbf{Q} = \sum_i p_i \boldsymbol{\psi}_i \boldsymbol{\psi}_i^*. \tag{2.3}$$

This example can be extended to the case in which the prepared state has a continuous distribution and ensures that measurement probabilities are properly modeled. A state with a rank-one density matrix is known as a *pure state* and corresponds to the case of no classical uncertainty about the prepared state. A state with a higher-rank density matrix is known as a *mixed state* [62].

Systems of many qubits can be represented as extensions of a single-qubit system. Any normalized vector in $\mathbb{C}^{2^n}$ is a valid multi-qubit state vector. States which are expressible as the Kronecker product of n single-qubit states are called *separable states*. The vector space of separable states is $\mathbb{C}^2 \otimes \mathbb{C}^2 \cdots \otimes \mathbb{C}^2$. For example, if $\mathbf{q}_1$ and $\mathbf{q}_2$ are single-qubit systems, the two qubit composite system is given by $\mathbf{q}_1 \otimes \mathbf{q}_2$. Analogously, if $\mathbf{Q}_1$ and $\mathbf{Q}_2$ are density matrix representations of two systems, the composite system has a density matrix of

$\mathbf{Q}_1 \otimes \mathbf{Q}_2$. States which do not admit this decomposition are said to be *entangled states*. Any positive semidefinite operator with a trace equal to unity is a valid density operator. In multi-qubit systems, observables and measurements are simply defined in the relevant higher dimensional space.

The *fidelity* provides a notion of distance between quantum states [62]. The fidelity function $F(\mathbf{Q}_1, \mathbf{Q}_2) \in [0, 1]$ is a symmetric function of its density matrix arguments. It is defined, for general mixed states as $F(\mathbf{Q}_1, \mathbf{Q}_2) = \mathrm{tr}((\mathbf{Q}_1^{\frac{1}{2}} \mathbf{Q}_2 \mathbf{Q}_1^{\frac{1}{2}})^{\frac{1}{2}})$ [62]. A low fidelity implies that states are "far apart," and the fidelity is equal to unity if its arguments are the same. The fidelity between two pure states is

$$F(\mathbf{q}_1, \mathbf{q}_2) = |\mathbf{q}_1^* \mathbf{q}_2|. \tag{2.4}$$

The fidelity between a pure state $\mathbf{q}$ and a mixed state $\mathbf{Q}$ is $F(\mathbf{q}, \mathbf{Q}) = \sqrt{\mathbf{q}^* \mathbf{Q} \mathbf{q}}$. The fidelity can be used to induce a metric on states, d, via $d(\mathbf{Q}_1, \mathbf{Q}_2) = \arccos(F(\mathbf{Q}_1, \mathbf{Q}_2))$ [62].

2.2 Quantum Gates

Gate-based quantum computers use *quantum gates* to transform quantum information. Quantum gates can act on a single qubit or on multiple qubits. In the single-qubit case, any unitary transformation of a single qubit is a valid quantum gate acting on that qubit [62]. Multi-qubit gates transform states comprised of multiple qubits, and are also encompassed by unitary transformations of the form $\mathbf{U} \in \mathbb{C}^{2^n \times 2^n},\ \mathbf{U}^* \mathbf{U} = \mathbf{I}_{2^n},\ n > 1$. A special class of multi-qubit gates are *controlled-*$\mathbf{U}$ *gates*, which act on two qubits. In a

controlled gate operation, one qubit acts as a *control qubit*, and the gate $\mathbf{U}$ is applied to the *target qubit*. The general form of a controlled-$\mathbf{U}$ gate on a two-qubit system $\mathbf{q} \otimes \mathbf{p}$, with control qubit $\mathbf{q}$ and target qubit $\mathbf{p}$ is

$$\mathbf{cU} = \begin{pmatrix} 1 & 0 & 0 & 0 \\ 0 & 1 & 0 & 0 \\ 0 & 0 & U_{00} & U_{01} \\ 0 & 0 & U_{10} & U_{10} \end{pmatrix} \tag{2.5}$$

Sequences of quantum gates are used to manipulate quantum information in the pursuit of a computational solution to a problem.

A *universal set* of quantum gates is a set of gates for which it is possible to express any unitary operation as a sequence of elements from that set. One such set of universal quantum gates consists of two single-qubit quantum gates and one controlled gate, namely,

$$\mathbf{H} = \frac{1}{\sqrt{2}} \begin{pmatrix} 1 & 1 \\ 1 & -1 \end{pmatrix}, \quad \mathbf{T} = \begin{pmatrix} 1 & 0 \\ 0 & e^{j\pi/4} \end{pmatrix}, \quad \mathbf{cX} = \begin{pmatrix} 1 & 0 & 0 & 0 \\ 0 & 1 & 0 & 0 \\ 0 & 0 & 0 & 1 \\ 0 & 0 & 1 & 0 \end{pmatrix}, \tag{2.6}$$

where the $\mathbf{cX}$ gate is known as the controlled-NOT gate [62].

2.3 Stabilizer Codes

Stabilizer codes are a class of quantum error correcting codes designed to protect against a wide range of quantum errors [24]. Their design is based on special properties of a matrix group defined for matrices of size $2^n \times 2^n$. We briefly summarize their construction.

The n-qubit Pauli group, $\mathcal{P}_n$, is the set of operators in $\mathbb{C}^{2^n \times 2^n}$ that can be written as a tensor product of n of the 2×2 Pauli matrices $\mathbf{I}, \mathbf{X}, \mathbf{Y}, \mathbf{Z}$, up

to a scalar multiple of $\alpha \in \{\pm 1, \pm j\}$, where

$$\mathbf{X} = \begin{pmatrix} 0 & 1 \\ 1 & 0 \end{pmatrix}, \quad \mathbf{Y} = \begin{pmatrix} 0 & -j \\ j & 0 \end{pmatrix}, \quad \mathbf{Z} = \begin{pmatrix} 1 & 0 \\ 0 & -1 \end{pmatrix}. \tag{2.7}$$

The group multiplication operation is defined as standard matrix multiplication. Elements of $\mathcal{P}_n$ are unitary and are either Hermitian or skew-Hermitian. Thus, they are orthogonally diagonalizable, with eigenvalues ± 1 or $\pm j$. Any two Pauli operators either commute or anti-commute. A stabilizer group, S, is a commutative (Abelian) subgroup of $\mathcal{P}_n$ that does not contain the negative of the identity element, $-\mathbf{I}_{2^n}$. Closure under the group multiplication operation implies that elements of S must have $\alpha = 1$. Thus, elements of S are Hermitian operators with eigenvalues equal to ± 1.

A *stabilizer code* $C(S)$ is defined as the subspace of $\mathbb{C}^{2^n}$ formed by the intersection of $+1$ eigenspaces of the operators in S. An efficient description of the group S is in terms of its generators. A set G_S of generators of S is a set of elements of $\mathcal{P}_n$ such that every element of S is a product of elements in G_S. A generator set G_S is called *independent* if the set obtained by removing an element from G_S fails to generate all elements of S. If S is a stabilizer with an independent generator containing $n-k$ elements, it can be shown that $C(S)$ is a 2^k dimensional vector space [62]. Furthermore, we also have that a state $\boldsymbol{\psi} \in C(S)$ if and only if $\mathbf{S}_n \boldsymbol{\psi} = \boldsymbol{\psi}$ for all $\mathbf{S}_n \in G_S$. Letting s_i denote complex constants and $\mathbf{v}_i$ an orthonormal basis for $C(S)$, a general *codeword* for $C(S)$ can be written as

$$\mathbf{x} = \sum_{i=0}^{2^k-1} s_i \mathbf{v}_i \ , \ \text{with} \ \sum_{i=0}^{2^k-1} |s_i|^2 = 1. \tag{2.8}$$

A codeword is thus an arbitrary unit vector in $C(S)$.

There are several criteria that can be used to determine which quantum errors a stabilizer code can correct. A simple approach, which we adopt, is as follows. Consider a set of error operators $E \subset \mathcal{P}_n$. Each error $\mathbf{E} \in E$ either commutes or anticommutes with each generator of the stabilizer group. A sufficient condition for the stabilizer code to correct the errors in E is for each $\mathbf{E} \in E$ to possess a unique commutation relationship with respect to the elements of G_S. Thus the stabilizer construction guarantees that each error $\mathbf{E}_k \in E$ maps the code space $C(G)$ bijectively to a 2^k dimensional subspace of $\mathbb{C}^{2^n}$. Furthermore, the uniqueness of the commutation relationships guarantees that different errors map $C(G)$ to different *error subspaces* ε_k. Formally, ε_k is the image of $\mathbf{E}_k$ restricted to $C(G)$ (i.e. $\varepsilon_k = \{\mathbf{y} \in \mathbb{C}^{2^n} \mid \exists\ \mathbf{x} \in C(G)$ with $\mathbf{y} = \mathbf{E}_k\mathbf{x}\}$) and a unique commutation relationship guarantees that $\varepsilon_k \cap \varepsilon_j = \varnothing$ when $i \neq j$. The error subspaces are uniquely identified during decoding by a *syndrome* (analogous to a classical syndrome), which are generated by performing projective measurements on the received state. In stabilizer coding, the syndromes are the eigenvalues associated with the outcome of the projective measurements applied during decoding.

It should be stated that this criterion is sufficient but not necessary; the stabilizer formalism naturally lends itself to *degenerate* quantum codes, where multiple errors yield the same syndrome and are correctable by the same operation. Consider a correctable error $\mathbf{E}$ and some $\mathbf{V} \in S$. Both $\mathbf{EV}$ and $\mathbf{E}$ will have the same commutation relations with respect to the stabilizer

generators, and thus both $\mathbf{EV}$ and $\mathbf{E}$ map an encoded state to the same subspace. Indeed, for $\mathbf{x} \in C(G)$ we have $\mathbf{EVx} = \mathbf{Ex}$; namely, the effect of the errors on the codeword is exactly the same.

In the quantum setting, the stabilizer decoding process consists of performing projective measurements on the received state.The measurement observables are the stabilizer generators. This process projects the state into an intersection of the $+1$ or -1 eigenspaces of each $\mathbf{S} \in G(S)$. Thus, after the measurements the state collapses into one of the error subspaces ε_k, and the syndromes resulting from the measurement identify the subspace. The error correction conditions guarantee that the application of a correction (e.g., the error operator itself) for any correctable error yielding the measured syndrome recovers the encoded state [24] [62]. This process demonstrates that a stabilizer code that can correct errors in a set E can correct an arbitrary linear combination of correctable errors [24]. The projective measurements annihilate error operators that are not consistent with the measured commutation relationship. For example, consider the state $\mathbf{y} = (c_j\mathbf{E}_j + c_k\mathbf{E}_k)\mathbf{t}$ with $\mathbf{t} \in C(S)$. If $\mathbf{G} \in G_S$ anti-commutes with an error $\mathbf{E}_j$ but commutes with $\mathbf{E}_k$ and a measurement of $\mathbf{G}$ returns a 1 (corresponding to a commutation), the state after measurement is $\hat{\mathbf{y}} = (\mathbf{I} + \mathbf{G})\mathbf{y} = \mathbf{E}_k\mathbf{t}$.

As we have detailed in this section, quantum error correcting codes like stabilizer codes include inventive encoding and decoding methods to account for the inherent system design limitations in quantum information processing. For example, both the no-cloning theorem and the projective measurement

process of observing a quantum state restrict quantum information processing approaches in a manner not found in a classical setting. Therefore, as we adapt these approaches to a classical setting, we leverage the fact that the limitations do not carry over and modify our analysis to account for the additional available information. In all of our designs, the key modifications we make to the standard quantum information processing approaches leverage techniques that go beyond what is possible in the quantum setting. Furthermore, our access to tools like nondestructive measurements and multiple copies of a state render the modified quantum information processing techniques more effective than they are when applied to true quantum systems.

Chapter 3

Quantum Emulation

Motivated by the difficulties in manipulating quantum physical systems for computing tasks, various architectures have been proposed for quantum computers, including gate-based [16], measurement-based [73], and quantum annealing systems [45]. Current quantum computing systems feature less than 100 qubits, and successful computation requires extremely careful isolation from environmental noise effects. The state of development has been termed the era of "noisy intermediate scale quantum computing" [67].

Extending on the work of [47], we have developed a prototype emulation approach to gate-based quantum computing based on an analog signal processing architecture. As we demonstrate in this section, the analog signal models in both the frequency domain and time-bin approaches are mathematically equivalent to the state of a multi-qubit gate-based quantum computer, presenting an opportunity to construct a system capable of manipulating quantum information using cheaper technology with access to more robust engineering

Portions of this chapter appeared in La Cour, Brian R., S. Andrew Lanham, and Corey I. Ostrove. "Parallel Quantum Computing Emulation." 2018 IEEE International Conference on Rebooting Computing (ICRC). IEEE, 2018. Authors contributed equally to these portions.

approaches. The model includes a scheme for initializing emulated quantum states, addressing and manipulating qubits with gate operations, and measuring the quantum state with outcomes determined by the Born rule [47]. This approach captures many advantages of quantum computers such as quantum parallelism and linear superposition without the need for substantial environmental isolation.

The quantum emulation device architecture is implemented using combinations of analog adders, multipliers, and filters with switching networks controlled by a digital microcontroller. In this section, we describe the mathematical representation of a gate-based quantum computer using an analog signal-based representation, revisiting the frequency-domain representation to motivate the system design approach. We then visit methods to encode information-carrying qubits in the time-domain, manipulate them, and we finally describe the hardware implementation used to realize the operations. Finally, we characterize the system performance with time-bin qubits using a slightly modified version of the fidelity performance metric tailored to the analog setting of our system.

3.1 Encoding Qubits in the Frequency Domain

In the signal-based quantum computing representation, a single-qubit system is defined as the vector space spanned by a pair of complex-valued functions in the vector space $L^2[0, T)$. In particular, the *standard computational*

basis functions for qubit k are defined as

$$\phi_0^{\omega_k}(t) = e^{j\omega_k t} \tag{3.1a}$$

and

$$\phi_1^{\omega_k}(t) = e^{-j\omega_k t} \tag{3.1b}$$

These basis elements are indexed using a binary representation, with $\phi_0^{\omega_k}(t)$ representing the 0 state of a qubit, and $\phi_1^{\omega_k}(t)$ representing the 1 state. Using the convention established in Equation (2.1) that the amplitudes defining the state of a qubit are normalized, the emulated representation of a single-qubit state $[\alpha, \beta]^T$ becomes

$$\psi(t) = \alpha\phi_0^{\omega_0}(t) + \beta\phi_1^{\omega_0}(t). \tag{3.2}$$

As described in Section 2, an n-qubit system lies in a vector space defined as the tensor product of the individual qubit systems. We introduce the convention that in an n-qubit quantum state, $\omega_0 < \omega_1 < \ldots < \omega_{n-1}$. Furthermore, we assume that the functions are defined only on the interval of the longest period, giving $T = \frac{2\pi}{\omega_0}$. A basis element for an emulated multi-qubit state is thus given as a product of n emulated single-qubit basis states. We extend the binary indexing to these n-qubit basis states by defining the index for a basis state to be $x = [x_{n-1} \ldots x_0]$, where x_i designate the binary values corresponding to the basis states of the individual qubits. An emulated multi-qubit basis state is thus

$$\begin{aligned} \phi_x(t) &= \phi_{x_n-1}^{\omega_n-1} \cdot \ldots \cdot \phi_{x_1}^{\omega_1}(t) \cdot \phi_{x_0}^{\omega_0}(t) \\ &= \exp\left[\sum_{i=0}^{n-1} j(-1)^{x_i}\omega_i t\right]. \end{aligned} \tag{3.3}$$

In terms of the underlying analog signals defined in (3.1a) and (3.1b), the multi-qubit basis states are complex sinusoids with frequencies given as the sum and differences of the individual qubit basis frequencies. To avoid overlaps of sums and differences, it is sufficient to assume an *octave-spacing scheme* for individual qubit bases, where $\omega_{k+1} \geq 2\omega_k$ for all k. The bandwidth utilization of the emulation device thus grows exponentially in the number of qubits. A multi-qubit quantum state can now represented as a linear combination of basis states. Letting x return the binary representation of an integer i, the analog signal is given as

$$\psi(t) = \sum_{i=0}^{2^n-1} \alpha_i \phi_{x(i)}(t). \tag{3.4}$$

To complete the Hilbert space representation of the quantum emulation device, we endow the space with an inner product. The inner product between two emulated quantum states $\varphi(t)$ and $\psi(t)$ is

$$\langle \varphi(t), \psi(t) \rangle = \frac{1}{T} \int_0^T \varphi^*(t)\psi(t)dt \tag{3.5}$$

The inner product is the output of a low-pass filter acting on the product of signals $\varphi^*(t)\psi(t)$. Under this inner product, any pair of distinct basis signals $\phi_x(t)$ and $\phi_{x'}(t)$ is orthonormal.

3.1.1 Gate Operations on Frequency Encoded Qubits

To achieve arbitrary gate-based transformations on emulated quantum states, a universal set of gates must be implemented. The prototype quantum emulation device supports arbitrary single-qubit unitary transformations and

the controlled-NOT gate, which constitutes a universal set of gates. The process of applying single-qubit quantum gates on frequency encoded qubits is described in detail in [47], and we briefly review it here. A general state $\psi(t)$ as in Equation (3.4) can first be decomposed along qubit k,

$$\psi(t) = e^{j\omega_k t}\psi_0^{(k)}(t) + e^{-j\omega_k t}\psi_1^{(k)}(t), \tag{3.6}$$

where $\psi_0^{(k)}(t)$ and $\psi_1^{(k)}(t)$ constitute the partial projections of $\psi(t)$ onto the zero and one state of qubit k. These two signals can be formed using networks of multipliers and bandpass filters as described in [47]. A single-qubit gate of the form

$$\mathbf{U} = \begin{pmatrix} U_{00} & U_{01} \\ U_{10} & U_{11} \end{pmatrix} \tag{3.7}$$

is applied to an emulated state by constructing the signal

$$\begin{aligned} \psi'(t) = [U_{00}e^{j\omega_k t} + U_{01}e^{-j\omega_k t}]\psi_0^{(k)}(t) \\ + [U_{10}e^{j\omega_k t} + U_{11}e^{-j\omega_k t}]\psi_1^{(k)}(t). \end{aligned} \tag{3.8}$$

Similarly, for a two-qubit controlled-gate operation, we let $\psi_{00}^{(k\ell)}(t)$, $\psi_{01}^{(k\ell)}(t)$, $\psi_{10}^{(k\ell)}(t)$, and $\psi_{11}^{(k\ell)}(t)$ denote the result of applying two projection operators as described in [47] onto control qubit k and target qubit ℓ, where the subscript denotes the state of the qubit for that projection. Since controlled gates apply only to the portion of the state where the control qubit is 1, a controlled gate

$$\mathbf{cU} = \begin{pmatrix} 1 & 0 & 0 & 0 \\ 0 & 1 & 0 & 0 \\ 0 & 0 & U_{00} & U_{01} \\ 0 & 0 & U_{10} & U_{11} \end{pmatrix} \tag{3.9}$$

is realized in the emulation device by creating the signal

$$\begin{aligned}\psi'(t) = \psi_{00}^{(k\ell)}(t) + \psi_{01}^{(k\ell)}(t) + [U_{00}e^{j\omega_\ell t} + U_{01}e^{-j\omega_\ell t}]\psi_{10}^{(k\ell)}(t) \\ + [U_{10}e^{j\omega_\ell t} + U_{11}e^{-j\omega_\ell t}]\psi_{11}^{(k\ell)}(t).\end{aligned} \tag{3.10}$$

3.2 Encoding Qubits in the Time Domain

Encoding qubits in the time domain affords a lower implementation overhead than the frequency-domain encoding methods described above while still allowing for frequency defined qubits. This significantly increases the number of available qubits at the cost of slower gate times. In this new encoding approach, the emulated quantum state for m time domain qubits spans $M = 2^m$ periods of length T, where T is the length of a frequency-domain encoded state. We now describe this encoding of m qubits in the time domain, which we term *time-bin encoding*, and show how both time-bin and frequency-based encoding can be used concurrently in constructing emulated quantum states.

The basis for a time-bin encoded qubit is defined using an m period time-shift operator $S_m : L^2(X) \mapsto L^2(X)$, where $X \subseteq \mathbb{R}$, that imposes a shift of mT. Specifically,

$$(S_m\psi)(t) = \psi(t - mT) \tag{3.11}$$

with the convention that $(S_m^0 f)(t) = f(t)$ and $(S_m^1 f)(t) = (S_m f)(t) = f(t - mT)$. Using this notation, we define a basis for a single ($m = 1$) time-bin encoded qubit k as a pair of shift operators mapping $L^2[0, 2^m T]$ to itself. The

operators act on the function $\varphi(t) = u(t) - u(t-T)$, yielding

$$\varphi_0(t) = (S_1^0\varphi)(t) = u(t) - u(t-T) \tag{3.12a}$$

and

$$\varphi_1(t) = (S_1^1\varphi)(t) = u(t-T) - u(t-2T). \tag{3.12b}$$

Arbitrary single-qubit states of the form $\boldsymbol{\psi} = [\alpha, \beta]^T$ obtain an emulated representation

$$\begin{aligned} \psi(t) &= \alpha\varphi_0(t) + \beta\varphi_1(t) \\ &= \alpha(S_1^0\varphi_0)(t) + \beta(S_1^1\varphi_0)(t). \end{aligned} \tag{3.13}$$

The inner product between arbitrary time-bin encoded single-qubit emulated states $\psi(t)$ and $\phi(t)$ is defined to be

$$\langle\phi(t), \psi(t)\rangle = \frac{1}{T}\int_0^{MT} \phi^*(t)\psi(t)dt. \tag{3.14}$$

Returning to multi-qubit states, we define the basis element for the binary state y of a time-bin encoded m-qubit state as the tensor product of the bases of the individual qubits. In this case, we define the tensor product space as the space generated by the bilinear function composition operator $\circ$. Letting $y = [y_{m-1}, \ldots, y_0]$, where again y_i are the binary values corresponding to the state of qubit i for that basis element, we have

$$\varphi_y(t) = \varphi_{y_{m-1}}(t) \otimes \varphi_{y_{m-2}}(t) \otimes \ldots \otimes \varphi_{y_0}(t) \tag{3.15a}$$

$$= (S_{2^{m-1}}^{y_{m-1}} \circ S_{2^{m-2}}^{y_{m-2}} \ldots \circ S_0^{y_0})\varphi_0(t). \tag{3.15b}$$

Multi-qubit time-bin states are thus a 2^m length sequence of DC signals. Letting $y(i)$ serve as a binary representation of an integer i, we have

$$\psi(t) = \sum_{y=0}^{2^m-1} \alpha_{y(i)}\varphi_{y(i)}(t). \tag{3.16}$$

The inner product between two multi-qubit states retains the form of Equation (3.14), where $\phi(t)$ and $\psi(t)$ are taken to be multi-qubit emulated systems. This completes the Hilbert space description of time-bin encoded quantum states.

3.2.1 Gate Operations on Time Encoded Qubits

Gate-based transformations of time-bin encoded qubits proceed in a manner similar to frequency domain gate processing. An m-qubit time-bin encoded quantum state $\psi(t)$ admits the following decomposition along a qubit k:

$$\psi(t) = \psi_0^{(k)}(t) + \psi_1^{(k)}(t) \tag{3.17}$$

Letting $b = [b_{m-1}b_m \dots b_0]$, the projected states are

$$\psi_0^{(k)}(t) = \sum_{b:b_k=0} \alpha_b\varphi_b(t) \tag{3.18a}$$

$$\psi_1^{(k)}(t) = \sum_{b:b_k=1} \alpha_b\varphi_b(t)\ . \tag{3.18b}$$

Each projection is a subsequence containing half the signals of the original time-domain sequence, and a value of zero elsewhere. With a single-qubit gate defined as in Equation (3.7), and defining $\bar{b}_k = [b_{m-1}, \dots b_{k+1}b_{k-1}, \dots b_0]$, that is, an $m-1$ bit binary index with the target qubit k's index removed, the

result of a gate operation on qubit k is given as

$$\begin{aligned}\psi'(t) = \sum_{\bar{b}_k} \Big(U_{00}\alpha_{[\bar{b}_k, b_k=0]}(t) + U_{01}\alpha_{[\bar{b}_k, b_k=1]}(t) \Big) \varphi_{[\bar{b}_k, b_k=0]}(t) \\ + \sum_{\bar{b}_k} \Big(U_{10}\alpha_{[\bar{b}_k, b_k=0]}(t) + U_{11}\alpha_{[\bar{b}_k, b_k=1]}(t) \Big) \varphi_{[\bar{b}_k, b_k=1]}(t)\end{aligned} \tag{3.19}$$

A controlled gate operation of the form given in Equation (3.9) with control qubit k and target qubit ℓ is realized in the following manner. Letting $\bar{b}_{k\ell}$ be the binary sequence b with b_k and b_ℓ removed, we have

$$\begin{aligned}\psi'(t) = &\sum_{\bar{b}_k} \alpha_{[\bar{b}_k, b_k=0]} \varphi_{[\bar{b}_k, b_k=0]}(t) \\ &+ \sum_{\bar{b}_{k\ell}} \Big(U_{00}\alpha_{\bar{b}_{k\ell}} + U_{01}\alpha_{\bar{b}_{k\ell}} \Big) \varphi_{\bar{b}_{k\ell}}\Big|_{b_k=1, b_\ell=0}(t) \\ &+ \sum_{\bar{b}_{k\ell}} \Big(U_{10}\alpha_{\bar{b}_{k\ell}} + U_{11}\alpha_{\bar{b}_{k\ell}} \Big) \varphi_{\bar{b}_{k\ell}}\Big|_{b_k=1, b_\ell=1}(t).\end{aligned} \tag{3.20}$$

3.2.2 Hybrid Emulated States

Emulated states consisting of both time-bin and frequency encoded qubits can be constructed and manipulated as well, exercising the advantages of each approach in tandem. These states exist in a vector space constructed as the tensor product of a time-bin system and a frequency encoded system. A basis element for the tensor product space of m time-bin qubits and n frequency-based qubits is represented as

$$\varphi_y(t) \otimes \phi_x(t) = S_{2^{m-1}}^{y_{m-1}} \circ S_{2^{m-2}}^{y_{m-2}} \ldots \circ S_0^{y_0} \left(\exp \left[\sum_{i=0}^{n-1} j(-1)^{x_i} \omega_i t \right] \right) \tag{3.21}$$

where y and x are the binary indices of the basis elements as defined in Sections (3.2) and (3.1). In this case, the tensor product is interpreted as the

action of the operator $\varphi_y(t) = S_y(t)$ on the function $\phi_x(t)$. It can be verified once again that this map is bilinear and hence constitutes a valid tensor product. With this interpretation, a hybrid time-frequency based quantum state is represented as

$$\psi(t) = \sum_b \sum_v \alpha_{b,v}(\varphi_v(\phi_b(t))) \ . \tag{3.22}$$

3.3 System Design and Performance

In this section we describe the hardware and firmware platform used to develop a prototype of the quantum emulation device. We constructed the device using standard analog electronic components controlled first by National Instruments analog and digital output modules on breadboards, and then with an STM32F4 series microcontroller, with all components mounted on printed circuit boards. The resultant two frequency qubit system is capable of generating arbitrary input states and manipulating them with single-qubit and controlled gate operations, with additional hardware for time-bin qubit processing.

3.3.1 Signal Generation and Capture

The system uses a dual-rail implementation of complex valued signals, where real and imaginary components are distinct and routed separately. Input emulated states $\psi(t)$ are generated by a pair of Texas Instruments DAC8831 digital-to-analog converters (DACs) operating at sample rate $f_s = 94,000$ Hz using the serial peripheral interface (SPI), one for the real component and

one for the imaginary component. The DACs operate in a bipolar configuration detailed in Figure 3.1. First, one period of the input signal is generated digitally. This signal is related to its analog counterpart (Equation (3.4)) by

$$\{\psi[n]\}_{n=0}^{K-1} = \psi(nT) \tag{3.23}$$

where $\omega_0 = 2\pi(1000)$, $T = 1/f_s$ and $K = \frac{2\pi f_s}{\omega_0}$. The digital samples are then converted into a 16-bit representation and transmitted serially to the DAC8831 devices using circular direct memory access (DMA) buffers to output multiple periods, if desired. The data converters perform the analog conversion, generating $\psi(t)$.

Transformations $\psi'(t)$ of input states $\psi(t)$ are captured with a pair of ADS8634 analog-to-digital converters (ADCs), depicted in Figure (3.2), after the application of either one gate or one controlled gate and analyzed using a modified fidelity metric based on the inner product of the sampled input and transformed signals. The ADCs use successive approximation registers controlled again by an SPI interface and operate at the same sample rate f_s as their DAC counterparts. The captured transformed signal is a sampled version of its analog counterpart in the same manner as was seen in Equation (3.23) for the generated signal, that is, $\{\psi'[n]\}_{n=0}^{K-1} = \psi'(nT)$.

Since the transformed and noise corrupted signal $\psi'(t)$ is not normalized, we define the fidelity using a modification of Equation (2.4). We let $\tilde{\boldsymbol{\psi}}$ and $\boldsymbol{\psi}'$ denote the two K-length sampled sequences in $\mathbb{C}^K$ to be compared.

The fidelity is then defined as

$$F(\tilde{\boldsymbol{\psi}}, \boldsymbol{\psi}') = \frac{|\tilde{\boldsymbol{\psi}}^* \boldsymbol{\psi}'|}{\big(||\tilde{\boldsymbol{\psi}}||_2\big)\big(||\boldsymbol{\psi}'||_2\big)} \tag{3.24}$$

This normalizes each received signal and the fidelity retains its interpretation as a measure of the closeness between emulated states, taking values on the interval $[0, 1]$.

Emulated quantum states that include m time-bin qubits are generated and captured by outputting $M = 2^m$ distinct signals of K samples each. In our implementation, this is achieved in a manner similar to the case with no time-bin qubits, except now the sampled input sequence is defined as $\{\psi[n]\}_{n=0}^{KM-1}$. The initial state after digital to analog conversion assumes the form given by Equation (3.22).

3.3.2 Time-Bin Gate Implementation

The time-bin gates described in Section 3.2.1 are implemented using a network of analog multiplier and adder components, along with an Analog Devices AD5724, (Figure (3.3)), to generate the DC gate coefficients. Unlike in the frequency-domain qubit setting, where analog processing is employed to create projected states corresponding to the states of the target qubit, the projected time-bin signals $\psi_0^{(k)}(t)$ and $\psi_1^{(k)}(t)$ are constructed without analog processing of $\psi(t)$. Instead, directly generate the projected signals $\psi_0^{(k)}[n]$ and $\psi_1^{(k)}[n]$ digitally, each projection a subsequence of the full time-domain sequence.

A time-bin gate is applied in five stages. In the first stage, the signals $\psi_0^{(k)}(t)$ and U_{00} are simultaneously generated and multiplied together with a network of AD826ANZ four quadrant multipliers, with the output $U_{00}\psi_0^{(k)}(t)$. For the next three stages, the process is repeated with the pairs U_{10} and $\psi_0^{(k)}(t)$, U_{01} and $\psi_1^{(k)}(t)$, and U_{11} and $\psi_1^{(k)}(t)$. Finally, in the fifth stage, the signals captured in stages 1-4 are regenerated and added together with the AD633 device. The sum corresponds to the transformed state $\psi'(t)$, as defined in Equation (3.19), which is resampled digitally. The circuitry performing the time-bin processing is depicted in Figure (3.4)

3.3.3 Time-Bin Gate Performance

The fidelity measurements we report here were conducted for emulated quantum states using the fidelity metric defined in Equation (3.24), where $\boldsymbol{\psi}'$ is the sampled emulated state after a gate-based transformation and $\tilde{\boldsymbol{\psi}}$ is the expected emulated output for that same transformation. We performed fidelity measurements for single-qubit gate transformations of emulated states with two frequency defined qubits and m time-bin qubits, applying one thousand randomly selected gates to the computational zero state, with the target qubit selected randomly as well. We calculated the average fidelity of the output to an ideal, simulated transformation. The results are plotted below for $m = 1$ to $m = 9$ time-bin qubits. The plots demonstrate that time-bin qubits can be added and processed with relatively little effect on the overall fidelity for up to five time-bin qubits, offering the computational advantage of more qubits

with little sacrifice to performance. The processing time, however, increases exponentially with each additional time-bin qubit.

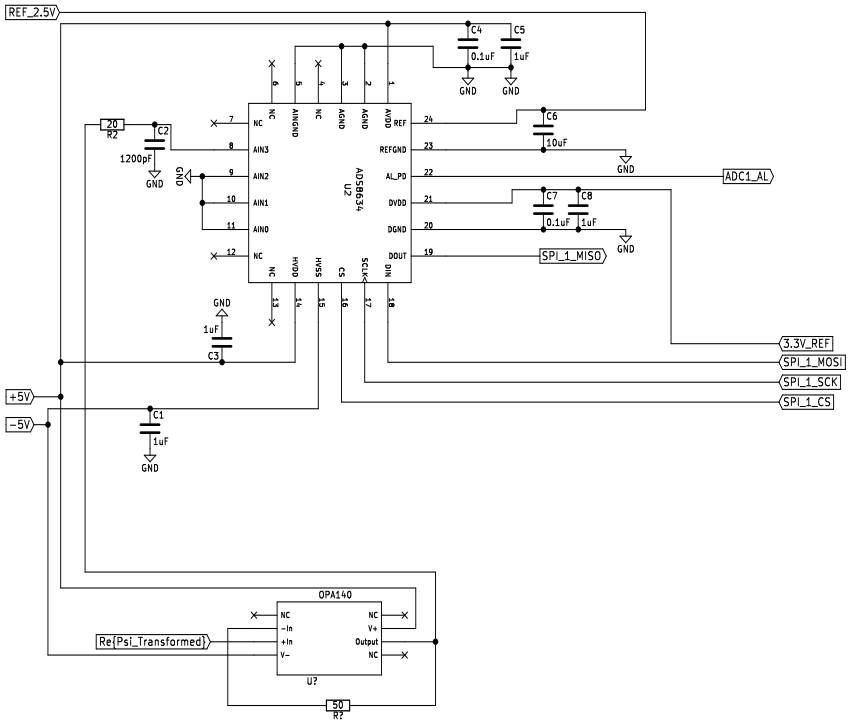

Figure 3.1: First of two schematic diagrams depicting the signal I/O. This figure depicts the bipolar ADC configuration. Only one ADC is depicted in the figure, but there are two in the prototype device, for real and imaginary.

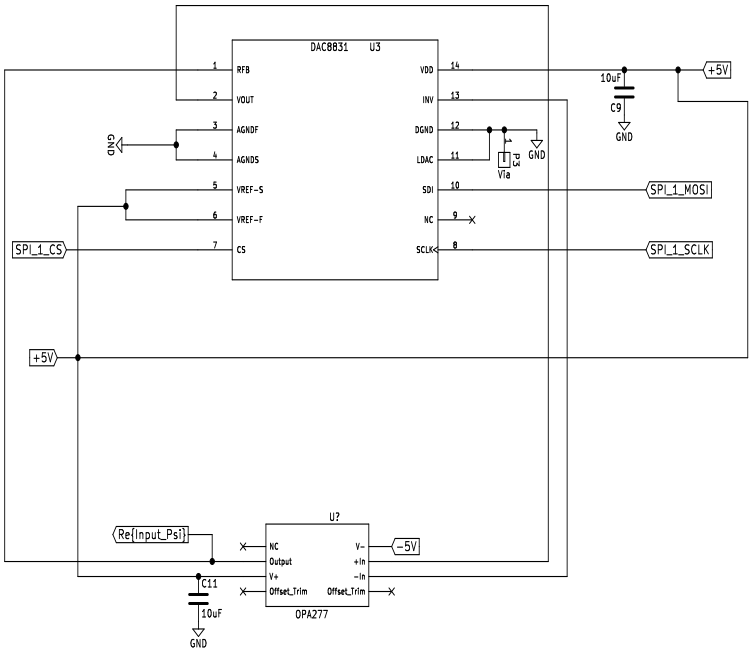

Figure 3.2: Second of two schematic diagrams depicting the signal I/O. This figure depicts the bipolar DAC configuration. Only one DAC is depicted in the figure, but there are two in the prototype device, for real and imaginary.

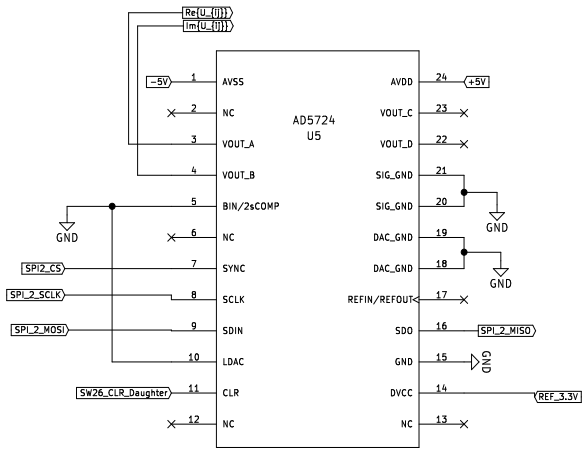

Figure 3.3: First of two schematic diagrams depicting the time-bin gate circuit. This figure depicts DAC that generates the DC coefficients for U_{ij}. The DC outputs of this DAC connect to the time-bin processing circuitry in the next figure.

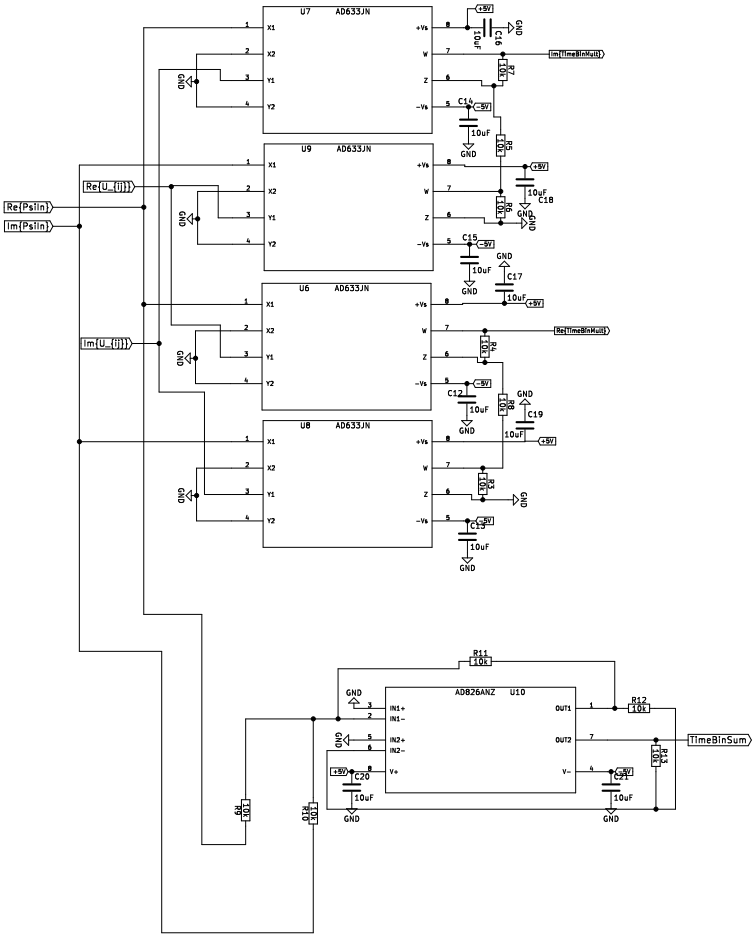

Figure 3.4: Second of two schematic diagrams depicting the time-bin gate circuit. This figure depicts time-bin processing circuitry. The AD826ANZ circuits perform four quadrant multiplication, and the AD633JN performs addition

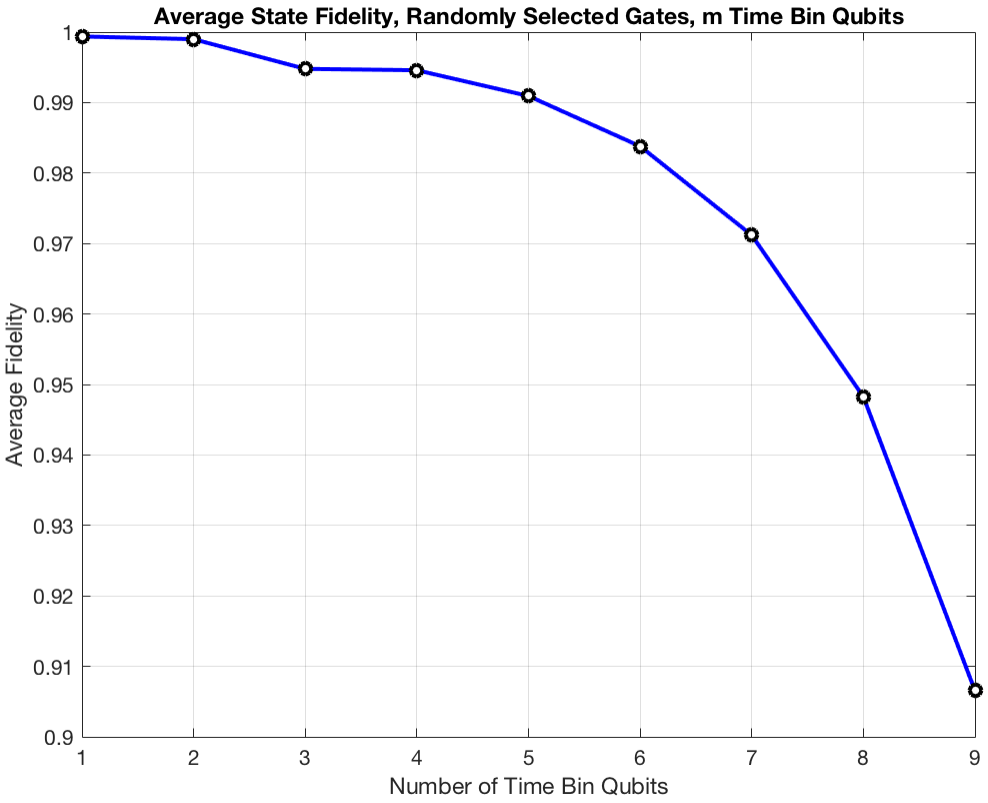

Figure 3.5: Average fidelity performance comparing emulation device output to simulated output for a random single-qubit gate applied to a randomly selected qubit in a hybrid emulated system with two frequency defined qubits and m time-bin qubits. The initial state is the computational zero state, and gates are chosen uniformly randomly by the Haar measure on $U(2)$.

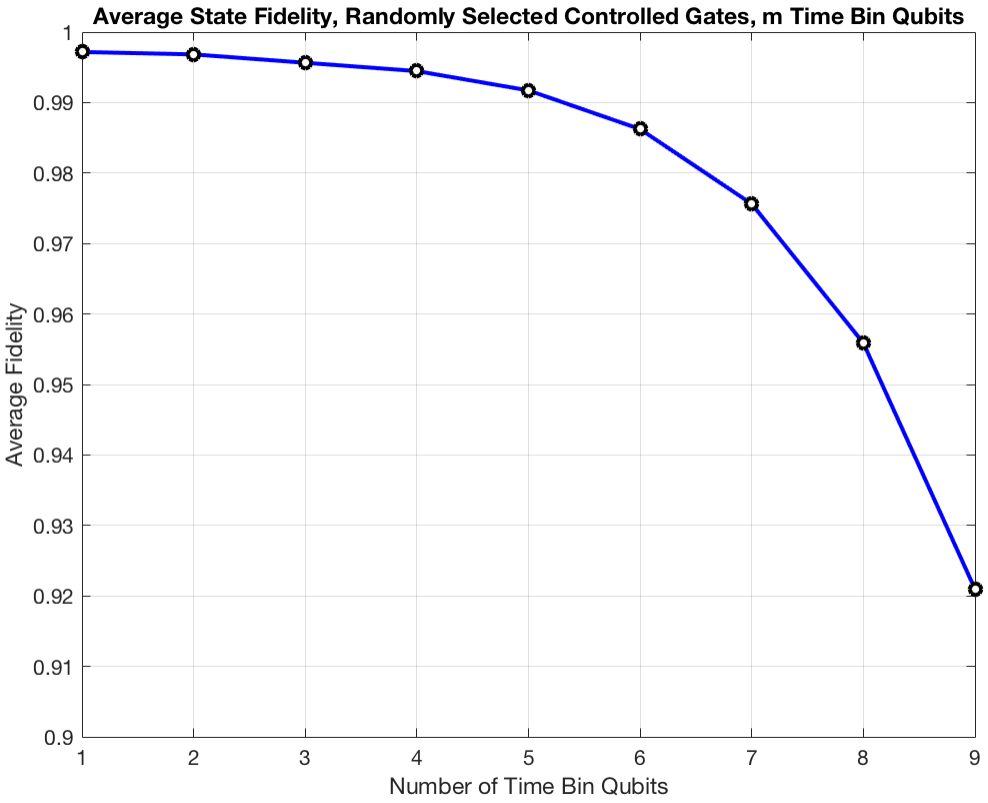

Figure 3.6: Average fidelity performance comparing emulation device output to simulated output for a random single-qubit controlled gate applied to a randomly selected qubit in a hybrid emulated system with two frequency defined qubits and m time-bin qubits. The initial state is the computational zero state, and gates are chosen uniformly randomly by the Haar measure on $U(2)$.

Chapter 4

Noncoherent Capacity Results

In the next two sections, we will analyze the information theoretic characterization and signal processing approaches for a constrained wireless communication setting called *noncoherent communication*. This will motivate the introduction of a stabilizer quantum error correcting code as a wireless communication signaling approach and invite a consideration of the similarities between quantum information and classical information. The structure of the adapted quantum code bears resemblance to the capacity-achieving approaches for the class of wireless classical communication channels reviewed in the next two sections, so the results presented here serve to provide context for the performance results in the final section.

Noncoherent wireless communication is characterized by a lack of channel state information (CSI) at both the transmitter and the receiver. While CSI is typically desirable for communication at high data rates, in certain scenarios its acquisition incurs excessive complexity or overhead, and the channel cannot be accurately estimated. This situation is encountered in various 5G paradigms. For example, channel estimation is difficult in high-mobility environments such as in high-speed trains or between aerial networks, where the

Doppler effect limits the coherence time of the channel [21, 99]. Similar limitations may be encountered in latency constrained environments, where the maximum blocklength is limited to ensure quick decoding, or in networks utilizing frequency hopping, which transmit sporadically at different times and frequencies [68, 88].

The objectives of 5G extend well beyond the enhancement of mobile broadband, additionally targeting massive machine-type communication (mMTC) and ultra reliable low-latency communication (URLLC) [3]. mMTC is characterized as communication in extremely dense networks of devices, for example, internet of things (IoT) networks communicating relatively small payloads intermittently and with high power efficiency [10]. URLLC refers to the transmission of data with stringent latency constraints at low error rates, which will enable 5G applications requiring mission-critical communication events such as autonomous vehicle networks [75]. These environments create extremely constrained communication scenarios, forcing the consideration of parameters such as blocklength and channel coherence time in extreme operating regions. Servicing demand for these new paradigms will require a thorough analysis of communication networks in nonstandard settings and motivates a reconsideration of noncoherent communication approaches.

4G systems have already partially addressed the demand for communication in fast fading and latency constrained scenarios. For example, the LTE-Advanced standard provides support for both low and high mobility users, with coverage for speeds up to 500 km/h [2]. The standard also provisions codes

with blocklengths as short as 100 symbols [1, Sec. 5.1.3]. Such efforts indicate a growing focus on restricted communication settings, and the objectives of 5G will target similar operating regimes with increased demands on reliable and high density communication. 5G networks will extend and advance these efforts by providing even greater reliability in these conditions.

In the past few years, researchers have made significant efforts toward creating analytical tools that capture all the tradeoffs between rate, reliability and latency in these settings. One such tool is the *maximal channel coding rate*, which integrates coherence time N_c, taken to be an integer number of symbol periods in a block fading model, blocklength, taken to be an integer multiple of the coherence time, $N = \ell N_c$, signal to noise ratio (SNR), where SNR $= \rho$, and probability of error p_e in the characterization of a communication environment [18]. For a symbol constellation of size M, the maximal coding rate can be expressed as

$$\begin{aligned} &R^*(\ell, N_c, p_e, \rho) \\ &\quad = \sup\left(\frac{\log(M)}{\ell N_c} : \text{a code exists for } (\ell, N_c, p_e, \rho)\right). \end{aligned} \tag{4.1}$$

Closed form expressions for R^* have not been found for even the simplest channel models, hinting at the difficulty of such a characterization, but many known results can be cast in terms of the maximal channel coding rate in various asymptotic regimes. The maximal channel coding rate provides a backdrop for the multifarious capacity results that exist for fading channels. We now visit some capacity expressions using this framework.

In this section, we set the stage to review the applicability of noncoherent signaling methods by visiting foundational capacity results for resource constrained environments. We make use of the maximal channel coding rate expression introduced above to introduce the results in the literature in a unified manner. We focus almost entirely on the frequency-flat setting, since most analysis in the literature is in this area.

4.1 Block Fading Models

For the purposes of narrowband modeling, it is extremely useful to take a time-varying baseband channel impulse response $h_b(t)$ and sample it at symbol rate T to obtain $h[n]$. A useful discretized model for the frequency flat channel is the *block-fading model*. In block-fading, the sampled channel impulse response $h[n]$ is assumed to be constant for N_c symbol periods, and then change independently to a new realization, where N_c is an integer. Given the maximum Doppler frequency ν_M in a channel experiencing Doppler shift, the coherence time is typically taken to be $T_c = \frac{1}{2\nu_M}$, satisfying the proportionality relation $T_c \propto \frac{1}{\nu_M}$. The additional adjustment factor of $\frac{1}{2}$ is chosen because it unifies the channel estimation minimum mean-squared error (MMSE) for the block-fading model with that of a continuous fading process with a rectangular Doppler spectrum [34]. In this way, the coherence time T_c of the continuous-time channel response can be converted to a coherence block of $N_c = \frac{T_c}{T}$ symbols for a discrete channel. This widely assumed model is the basis for many of the information-theoretic results for the noncoherent com-

munication environment [58, 97]. The assumptions of the model can also be relaxed to admit slightly different scenarios. For example, some block-fading models feature continuous variation within coherence blocks, but with hard transitions to independent values across blocks [52]. Others consider channels with correlations between separate channel realizations [44].

We can leverage the block fading model to derive the coherence interval of systems in motion. For example, consider a vehicle in communication with a stationary base station where the relative velocity between the two is $60\frac{\text{km}}{\text{h}}$. A signal at approximately the carrier frequency $f_c = 4$ GHz will experience a maximum Doppler shift of $\nu_M = f_c v/c \approx 222$ Hz. The corresponding coherence time is $T_c = \frac{1}{2\nu_M} \approx 2.25$ms. For a symbol period of $T = 5\mu s$, the coherence block is $N_c = T_c/T = 450$ symbols.

If we increase the velocity to $450\frac{\text{km}}{\text{hr}}$, a situation reflective of air-to-ground or air-to-air communication, the coherence time reduces to $N_c \approx 58$ symbols. At these velocities, the channel estimation overhead becomes much more pronounced and may merit a consideration of a noncoherent approach. Similarly, operation at higher carrier frequencies increases the intensity of the Doppler effect, also reducing the coherence time of the channel. This is especially prevalent at millimeter wave frequencies, where approaches that avoid estimating the channel at every coherence block have been explored [72, 89].

4.2 Noncoherent SISO Capacity Results in Rayleigh Fading

By far the most widely studied model in the noncoherent communication setting is the frequency flat block Rayleigh fading channel, often used to model a rich scattering communication environment. Numerical results for the ergodic capacity of such a setting were obtained first in the 1990's by exploiting the symmetry of Gaussian distributed matrices to simplify the mutual information expression. The capacity was numerically computed using the Blahut-Arimoto algorithm for the cases of one transmit and one receive antenna ($N_t = N_r = 1), N_c \geq 1$ [58]. This result corresponds to the regime

$$\lim_{\ell \to \infty} R^*(\ell, N_c, p_e = 0, \rho), \tag{4.2}$$

as do all ergodic capacity results in block fading. Notably, in this limit error-free communication is possible, so p_e can be made arbitrarily small. The SISO ergodic capacity-achieving input distribution of the block fading Rayleigh channel was later explored in more depth for the case of independent fading per symbol ($N_c = 1$), where it was found to always be discrete with finite support, reducing to an on-off signaling scheme for low-SNR communication ($\rho \to 0$) [4]. Analysis of the ergodic capacity at low SNR for a block-fading Rayleigh channel continued with [71] under peak constraints, where it was shown that capacity growth is quadratic with SNR in this region, indicating poor power efficiency at very low SNR. A high-SNR analysis of the block fading model found that for $N_c = 1$, the ergodic capacity grows only double-

logarithmically in the SNR; that is,

$$\lim_{\rho\to\infty}\lim_{\ell\to\infty} R^*(\ell, N_c = 1, p_e, \rho) = \log_2(\log(\rho)) + \mathcal{O}(1) \tag{4.3}$$

highlighting a similar power inefficiency of noncoherent communication in this region [51]. However, further analysis considered a Rayleigh fading process with a Gauss-Markov evolution to more accurately delineate the SNR region in which this asymptotic behavior is observed, finding that the double logarithmic growth rate results largely from the assumption of extreme, temporally independent, channel variation [20]. Because wireless channels are underspread, almost all communication systems operate in regions of slow channel variation, and in this case, increases in SNR continue to yield a logarithmic, rather than doubly logarithmic, growth in capacity. Nonetheless, the findings of [20] indeed confirm that for channels in which the fading variability is more significant than the noise, communication becomes extremely power inefficient.

Low SNR capacity characterizations were also considered in the SISO setting with applications to wideband channels. Initial results on the asymptotic behavior of the wideband capacity were established in the 1960s, where it was found that the noncoherent wideband capacity for Rayleigh fading is the same as the capacity of the wideband AWGN channel in the limit of large bandwidth [41]. The capacity-achieving distribution for such channels was later shown to rely on "flash signaling," characterized by the kurtosis of the input distribution growing unboundedly with the bandwidth [90]. With maximum constraints imposed on the kurtosis or on the power, the capacity in the

limit of bandwidth can instead be shown to be zero [60, 90].

To more accurately model realistic systems and avoid overly "peaky" signaling, noncoherent characterizations of capacity at low SNR continued to focus on settings with constraints on peak signal power or the kurtosis of the input distribution, in addition to the average signal power constraints. For example, an analysis at low SNR revealed that frequency shift-keying methods achieve the capacity up to a second order Taylor expansion of capacity, a result that also holds for the MIMO setting [82]. For block Rayleigh fading models with constraints on the fourth moment, the capacity growth at low SNR was again shown to be quadratic, indicating a slower growth than the linear growth observed in coherent channels for SNRs near zero [71]. Essentially, the lack of perfect channel knowledge has tremendous impact on the power efficiency in high noise (or low-power) environments, and it is largely ineffective to communicate noncoherently in this region, except in situations where the channel estimation overhead is negligible [90, 98]. At the same time, naive channel estimation strategies are typically unreliable in this setting as well; it may simply be impossible to attain anything resembling perfect channel state information at the receiver (CSIR). Low SNR analyses were also performed substituting block fading models for Gauss-Markov models to better understand slow time variation, where the capacity growth was also found to be either linear or quadratic in the SNR, depending on the power constraint imposed on the transmitter. [76].

Moving on from the wideband setting, the quasi-static capacity of the

noncoherent Rayleigh communication channel corresponds to the regime where $\ell = 1$ and $N_c \to \infty$, i.e.

$$\lim_{N_c \to \infty} R^*(\ell = 1, N_c, p_e, \rho) \tag{4.4}$$

Unsurprisingly, the capacity in this situation is equal to the capacity when the channel is perfectly known, since any channel estimation incurs a negligible overhead [58]. However, recent work has explored the capacity for communication over a single coherence interval, i.e., an analysis of R^* for $N_c < \infty$ and $\ell = 1$, which can also be regarded as a quasi-static regime, though at finite blocklength [94]. A different analysis must ensue for codes with finite blocklengths because for many models of interest, such as the AWGN environment, communication with vanishing probability of error is not possible. One reason for this can be explained using the concept of *information stability*. An information stable channel is characterized as a channel whose *information density*

$$i(\boldsymbol{s}; \boldsymbol{y}) = \log_2 \left(\frac{f_{\mathbf{s},\mathbf{y}}(\boldsymbol{s}; \boldsymbol{y})}{f_{\mathbf{s}}(\boldsymbol{s}) f_{\mathbf{y}}(\boldsymbol{y})} \right) \tag{4.5}$$

does not deviate from the mutual information $I(\boldsymbol{s}; \boldsymbol{y})$ in the limit of large blocklength. That is,

$$\lim_{N_c \to \infty} \frac{1}{N_c} i(\boldsymbol{s}; \boldsymbol{y}) = \lim_{N_c \to \infty} \frac{1}{N_c} I(\boldsymbol{s}; \boldsymbol{y}) \tag{4.6}$$

For finite blocklengths, this relation does not hold, and the information density may fluctuate around the mutual information $I(\boldsymbol{s}; \boldsymbol{y}) = \mathbb{E}[i(\boldsymbol{s}; \boldsymbol{y})]$. Thus the channel capacity must instead be characterized using the statistics of the

information density rather than the mutual information. Furthermore, a target probability of error must specified, since error-free communication is no longer possible.

Defining the variance of the information density to be

$$V = \mathrm{var}[i(\mathbf{s};\mathbf{y})], \tag{4.7}$$

the maximum spectral efficiency is newly defined by admitting a maximum tolerable probability of decoding error p_e and adding terms that capture the backoff from the asymptotic capacity. The expression is

$$\frac{R}{B} = C - \sqrt{\frac{V}{N_c}} Q^{-1}(p_e) + \mathcal{O}\left(\frac{\log N_c}{N_c}\right) \tag{4.8}$$

where Q^{-1} refers to the Gaussian Q function and C is the capacity of the channel in the limit of blocklength [65]. Due to the $\mathcal{O}(\frac{\log N_c}{N_c})$ factor in the expression, Equation (4.8) is still most accurate for large blocklengths. However, this expression provides a more accurate view of the achievable spectral efficiency for channels with finite blocklengths and has led to a surge of new results in information theory. The result of Equation (4.8) can be applied in the characterization of a quasi-static noncoherent channel with $\ell = 1$ and $N_c < \infty$ [66]. For both SISO and MIMO communication in Rayleigh fading, even at finite blocklength, the asymptotic outage capacity was shown to effectively serve as a proxy for the finite blocklength outage capacity, indicating that outage events are the main impediment to high-rate communication in the quasi-static regime [94]. This also establishes the continued effective-

ness of codes mitigating against outage events at finite blocklengths, such as space-time codes.

4.3 Noncoherent MIMO Capacity Results in Rayleigh Fading

We now turn to a treatment of the capacity of a multiantenna communication setup. The work of Marzetta and Hochwald provided the first thorough treatment of the noncoherent ergodic capacity of multiple antenna channels with N_t transmit antennas and N_r receive antennas, giving numerical results for selected values of $N_t, N_r \geq 1$, $N_c \geq 1$ at all SNRs and characterizing the signaling structure for the general case. Zheng and Tse, building on this initial work, characterized the noncoherent ergodic capacity for a Rayleigh fading channel in the high SNR regime for $\frac{N_c}{2} \geq N_t + N_r$ [97]. These results correspond to

$$\lim_{\ell \to \infty} \lim_{\rho \to \infty} R^*(\ell, N_c, p_e = 0, \rho) \tag{4.9}$$

and the given capacity expression is

$$R^* = N_t(1 - \frac{N_t}{N_c}) \log(\rho) + \mathcal{O}(1). \tag{4.10}$$

The double logarithmic growth in the capacity at high SNR discussed for SISO Rayleigh fading was also reestablished for the multiantenna setting with extreme temporal channel variation. Moreover, the addition of antennas at either transmitter or receiver was found not to improve this asymptotic behavior [51]. However, the previous discussion of the interplay between channel variability

and noise also applies here, and for most SNRs of interest in underspread wireless communication channels, the high SNR capacity of a noncoherently communicating multiantenna system is given by Equation (4.10).

Another important result for the noncoherent MIMO communication environment extends the high-SNR capacity expression in Equation (4.10) to the case when $N_t \leq \min\{N_r, \lfloor \frac{N_c}{2} \rfloor\}$, allowing for an analysis of the ergodic capacity for cases when $N_c \leq N_t + N_r$ [95]. The capacity in this situation is

$$R^* = N_t(1 - \frac{N_t}{N_c}) \log(\rho) + c + o(1) \tag{4.11}$$

where c is given as in [95, Eq. 9]. This is useful for capacity analysis of communication systems with large receive arrays. The capacity results above were expanded upon by further asymptotic characterizations for non-block fading models in narrowband channels, where it was shown that for Rayleigh fading channels with correlated variation within an interval N_c, but independence between intervals, and covariance matrix of rank Q, the capacity is lower bounded at high SNR by

$$R_\ell^* = T^*(1 - T^*Q/N_c) \log(\rho) + \mathcal{O}(1) \tag{4.12}$$

where $T^* = \min\{N_r, N_t, \lfloor N_c/(2Q) \rfloor\}$ [52]. These results point to the overall usefulness of multiple antennas in increasing the capacity in noncoherent communication environments at high SNR.

Many of the wideband analyses performed in the SISO regime extend to the MIMO setting. For example, the capacity growth rates at low SNR are similar but can be improved upon by adding more antennas. In both block

fading and Gauss-Markov fading, the capacity of a wideband channel at low SNR increases linearly with the number of receive antennas and quadratically with the number of transmit antennas [76, 92]. Since peak power constraints are imposed on individual antennas, the addition of more transmit antennas under an average power constraint allows for signaling schemes with higher kurtosis. Initially, it was believed that only one transmit antenna should be used for low SNR signaling, but later analyses derived signaling using all transmit antennas [82].

4.4 Other Noncoherent Capacity Results

Computing the capacity of a noncoherent channel is typically intractable without significant simplifications, and for this reason results for channels other than the Rayleigh fading are sparse. However, there are analyses applicable to entire classes of stochastic channel models characterizing global properties of the input distribution in various operating regions. For example, it has been discovered that for most communication in low SNR environments, the optimal input distribution is discrete with finite support [38]. Another general treatment of the noncoherent capacity, this one applying to underspread wide-sense stationary uncorrelated scattering (WSSUS) channels, as given in [19], establishes that coarse bounds for the channel capacity can be determined based only on the channel scattering function and peak-power constraints, growing tighter as the operating bandwidth grows.

Returning to specific channel models, some results characterizing the

tradeoff between spectral efficiency and bit-energy in the SISO noncoherent Rician fading channel have been obtained in the low-SNR limit, where first-order approximations of the capacity are accurate [26, 27]. Similarly, general properties of the capacity-achieving input distribution in Ricean fading, such as the cutoff rate, have been analyzed [50].

In the next section, we continue our analysis by reviewing noncoherent signaling approaches inspired by the capacity-achieving input distributions detailed in this section. Often, the capacity-achieving input distribution must either be significantly modified or otherwise be very crudely approximated to satisfy system and signal processing limitations which do not fully factor into the information-theoretic characterization of a communication link. Furthermore, the enticing spectral efficiency implied by such capacity-inspired approaches may give rise to undesirable secondary effects like highly inefficient decoders. We outline how the literature has addressed these concerns, first presenting the capacity-inspired signaling and then visiting modifications and alternative approaches.

Chapter 5

Noncoherent Signaling

Having established the known capacity results for noncoherent communication in a variety of environments, we now visit the signaling approaches associated with these capacity expressions and comment on their realizability from a signal processing perspective. We focus on signaling that is both inspired by the capacity-achieving distributions and informed by signal processing concerns such as receiver complexity. We focus on signaling in the fast fading regime, where channel estimation is either impossible or potentially suboptimal. Since many results for the capacity are asymptotic in SNR, we focus on signaling in the high and low asymptotic SNR regions separately.

5.1 SISO Signaling in Rayleigh Fading

The SISO fading setting with additive noise can be mathematically modelled by the equation

$$\boldsymbol{y} = \sqrt{\rho} h \boldsymbol{x} + \boldsymbol{n}. \tag{5.1}$$

where $\boldsymbol{y}, \boldsymbol{x}$, and $\boldsymbol{n}$ are all $N_c \times 1$ length vectors. Consider the information carrier of the channel, the input $\boldsymbol{x}$. Depending on the SNR characteristics of a fading channel, it is useful to consider it in terms of its magnitude and direc-

tion components $\boldsymbol{x} = |\boldsymbol{x}|\hat{\boldsymbol{x}}$. From the perspective of achieving capacity, each component is differently emphasized in the two SNR regimes. This represents a departure from the capacity behavior of non-fading AWGN channels, where the capacity-achieving input distribution is the same with SNR. In contrast, for the low SNR regime in frequency flat fading, the information carried by the input is encoded in the magnitude of $\boldsymbol{x}$, and the signaling structure resembles on-off keying. As the coherence time grows, the symbol energy becomes more evenly distributed across the coherence interval, until energy is evenly distributed in each time interval [4]. As $\rho \to \infty$, to contrast, the information is entirely carried in the unit vector $\hat{\boldsymbol{x}}$. This is because the noise can essentially be neglected at high SNR, thus the effect of the channel is to rotate $\hat{\boldsymbol{x}}$ by a global phase constant and scale by some magnitude. This can be seen by observing that $h = |h|e^{j\theta_h}$, giving $\boldsymbol{y} \approx |h|e^{j\theta_h}\boldsymbol{x}$. Since magnitude and global phase do not affect information encoded in the unit vector, information is perfectly preserved. We now visit signaling approaches derived from these insights in more depth.

As previously mentioned, capacity at extremely low SNRs is achieved by arbitrarily increasing the maximum power, or peak, of the "on" signal as the SNR decreases. Since realistic signaling includes some sort of constraint on the peak power, approaches based on peaky signaling must take these power constraints into account, which significantly changes the attainable rates of the system, especially in wideband channels [90]. Power limitations of the communication hardware are typically accounted for in the form of a fourth

moment constraint, a per-antenna power constraint, a peak power constraint, or a peak to average power ratio constraint. Notably, introducing these constraints prevents communication at the minimum bit energy to noise ratio $\frac{E_b}{N_0}$ as $\rho \to 0$ [60].

Noncoherent signaling for the low SNR setting includes M-ary frequency shift keying (MFSK), since it is known to achieve the first order capacity expansion at low SNR [41, 64]. MFSK has also been found to be optimal for certain continuous-time time-varying fading models [86]. In wideband settings, MFSK can be combined with on-off keying to achieve peaky signaling in both time and frequency, subject to appropriate power constraints [28]. At high SNR, by contrast, signaling reverts to single-antenna unitary modulation, where a packing of $N_c \times 1$ complex vectors is chosen as the codebook [58]. Decoding for these codebooks is exponential in the rate, as the correlation between the received signal and each vector in the codebook must be calculated. In contrast to this high complexity decoding, channel estimation and equalization is extremely simple and accurate in high SNR SISO communication, rendering noncoherent approaches unpopular in the single antenna setting.

5.2 MIMO Signaling in Rayleigh Fading

We now visit signal processing approaches in the Rayleigh faded MIMO setting. This situation is modelled by

$$\boldsymbol{Y} = \sqrt{\frac{\rho}{N_t}}\boldsymbol{H}\boldsymbol{X} + \boldsymbol{N} \tag{5.2}$$

where $\boldsymbol{X} \in \mathbb{C}^{N_t \times N_c}$, $\boldsymbol{H} \in \mathbb{C}^{N_r \times N_t}$, and $\boldsymbol{Y}, \boldsymbol{N} \in \mathbb{C}^{N_r \times N_c}$. As in the SISO setting, the capacity is achieved using different signaling methods at high SNR than at low SNR, so we visit each case separately. Generally, the capacity-achieving approach at high SNR is unitary space-time coding (USTC), while at low SNR, it is better to use peaky orthogonal signaling, such as MFSK or on-off keying.

In the low SNR setting, the suboptimality of treating channel estimates as perfect was established from an information-theoretic standpoint [71]. Initially, it appeared that low SNR operation should always revert to signaling with a single transmit antenna [36], but by integrating peak power constraints and removing assumptions on the capacity-achieving signal structure, it was later proven that additional transmit antennas can be employed to improve communication. Specifically, the peak power constraint typically applies per-antenna, which does not preclude the opportunity for more total power to be transmitted by using more antennas under an average power constraint. The optimal signaling uses all available transmit antennas, performing best when the codewords $\boldsymbol{X} \in \mathbb{C}^{N_t \times N_c}$ are chosen to be rank-1 matrices, and the approach is termed space-time rank-one orthogonal modulation (STORM) [82]. We examine the performance of this approach in comparison to one that estimates the channel at low SNR in Figure (5.1). The choice of rank-one codewords can be interpreted as a way to reduce the number of unknown path gains from $N_r N_t$ to N_r, which can be used to lessen the implicit channel estimation overhead. The resulting modulation resembles MFSK, but with an on-off keying modi-

fication, since a transmission of zero power is a valid symbol. For extremely low SNRs the approach reverts to a simple on-off keying, as is optimal for that setting [71]. The transmission of rank-one space-time codewords benefits from full correlation in both the transmit and receive antenna structures [9]. Receiver designs optimized for low SNR focus on parameters besides capacity such as pairwise error probability [9] and receiver complexity. Receiver structures for FSK based signaling have been proposed that reduce the complexity by leveraging the fast Fourier or Hadamard transform [82]. Another structure exploits a relation between the pairwise error probability and the Kullbeck-Liebler divergence to inform the design of space-time constellations based on the latter quantity between conditional distributions [11]. Codes using transmit beamforming were also proposed for correlated Rayleigh fading at low SNR [81].

Code designs for the high-SNR environment rely on a markedly different structure than the peaky orthogonal signaling discussed so far for low SNR. As was established in [58] the capacity-achieving signaling code matrix $\boldsymbol{X}$ is the product of an isotropically distributed unitary $N_t \times N_c$ matrix $\boldsymbol{\Psi}$ and an independent $N_t \times N_t$ real, nonnegative diagonal matrix $\boldsymbol{V}$, that is $\boldsymbol{X} = \boldsymbol{V}\boldsymbol{\Psi}$. A random matrix is isotropically distributed if its probability density is not changed when it is multiplied by a unitary matrix. One of the first noncoherent code designs exploited knowledge of this structure and attempted to emulate it tractably. Termed unitary space-time coding (USTC), the constellation consists of L semi-unitary $N_t \times N_c$ matrices $\{\boldsymbol{\Phi}_j\}_{j=1}^{L}$ all scaled by the same

factor $\sqrt{N_c}$ [35]. While the decoding complexity of initial USTC designs are exponential in the rate and number of transmit antennas, the decoding is relatively simple, a contrast to Gaussian signaling that achieves capacity for unfaded additive noise channels. An early unitary space-time codebook design used tight frames based on the discrete Fourier transform as codewords, leading to block-circulant correlated codes [36]. Followup analysis of the high SNR capacity demonstrated that the transmit matrix $\boldsymbol{X}$ is distributed uniformly on the Grassmann manifold, that is, the set of M dimensional subspaces of $\mathbb{C}^T$, and presented a sphere packing argument in this geometric setting [97]. These two results led to intense focus on codebook designs as packings on the Grassmann manifold, and many of the approaches we visit are based on this intuition.

Approaches using Grassmannian packings focus on optimizing the distance between points on the Grassmann manifold with respect to some distance metric. The metric used depends on the objective, which is typically some measure of diversity. Diversity arises in minimizing the pairwise error probability between two codewords. The sum and product diversity are defined based on expressions that appear in the Chernoff bound on probability of symbol decoding error in the noncoherent setting: Let $\boldsymbol{U}_1$ and $\boldsymbol{U}_2$ be two codewords in a space-time code and d_i^2 be the squared singular values of the product $\boldsymbol{U}_1^*\boldsymbol{U}_2$. Then the *product diversity* is defined as

$$D_{\mathsf{prod}} = \Pi_j(1 - d_j^2) \tag{5.3}$$

and is useful for minimizing the bit error probability at high SNR [35], while the *sum diversity* is defined as

$$D_{\mathsf{sum}} = \sum_j (1 - d_j^2) \tag{5.4}$$

and is better suited to minimize the bit error probability at low SNR [29].

Interestingly, when the space-time codewords are points on the Grassmann manifold, the sum diversity is intimately related to a metric known as the *chordal distance* on this space. Maximizing sum diversity therefore reduces to a problem of finding maximally separated points with respect to this metric. Codebook designs based on the chordal distance can be found in [5, 8, 36, 96]. Similarly, space-time codes designed for low probability of error at high SNR are designed to minimize the product diversity (e.g. [32, 35]). Other codes use different metrics to design codes. For example, observing that codebooks designed with respect to the chordal distance do not guarantee full diversity space-time codes, [59] proposed a design based on a different metric on the Grassmann manifold inspired from the asymptotic union bound. Some full diversity designs occur entirely in the geometric setting, potentially sacrificing a unitary codebook [63,93]. Other code designs move away from the focus on diversity, instead leveraging transformations to create unitary codes. Examples include an approach leveraging the Cayley transform to transform dispersion codes into unitary codes [31], and an exponential map transforming space-time codes into unitary codebooks [46], though these codes do not guarantee full diversity.

	Grassmannian	**Differential**	**Alamouti (Coherent)**	**STORM-FSK**
Optimal SNR Region	High	High	Moderate	Low
Receiver Complexity	High	Moderate	Low	Low
Coherence Time	Short	Short/Medium	Long	Short
Supportable Rates	High	Low	High	Low

Table 5.1: A summary of the performance of the MIMO noncoherent and coherent signaling approaches discussed. We examine the performance of each approach by characterizing where it attains its best performance with respect to reliability.

Receiver complexity varies for these approaches. Unitary space-time coding itself is exponential in both the encoding and the decoding, though this is improved to a polynomial encoding in [36]. Many other codes discussed require the generalized likelihood ratio test, which jointly calculates the likelihood ratio of both channel and data [5, 9, 46, 91]. This can also place a significant computational burden on the receiver. Other approaches simply use a maximum likelihood (ML) estimator simplified by the assumption of Rayleigh fading [59]. Many approaches exploit special structure of the codebook to reduce complexity and improve performance, such as the block circulant property [36], orthogonal designs (which effectively estimate the channel explicitly) [85, 96], Gray coding [14], and Reed-Muller coding [7, 8].

5.3 Differential Coding

Differential codes deviate from the signaling structures considered so far in that they do not rely on any particular statistical distribution of the fading in their construction, but only on the fading coherence. While extremely fast

fading may not provide enough coherence for differential encoding to excel, there is no reliance on channel estimates, which can reduce training overhead and complexity at the receiver. Lack of dependence on the channel statistics, however, means that differential codes do not resemble the capacity-achieving structures considered thus far. In differential coding, information is instead encoded in the relationship between successive transmissions. Numerous constructions exist for both the SISO and the MIMO setting.

Historically, SISO differential codes were used in early cellular standards such as IEEE IS-54 and certain voice-band modems, eventually falling into disuse in favor of approaches leveraging channel estimation. Almost all SISO differential codes are generalizations of differential phase shift keying, and so we focus on the multiantenna setting. Multi-antenna communication renewed interest in differential coding, leading to the design of differential codes exploiting the capacity and reliability improvements of MIMO. Differential coding is more recently being considered in the URLLC paradigm for vehicular communication [23]. Because they rely on channel coherence, differential codes appear to be better suited for moderate to high SNR communication and moderate to slow fading from a reliability perspective. We explore this prospect in the simulations of Figure 5.2.

Differential codes require the channel to be as close to constant as possible over many time slots, since information is encoded in a sequence of transmissions. Thus, fast fading environments can create challenging conditions for differential coding. Conversely, short blocks of differential codes may

indeed provide a useful alternative to long channel estimation times, but differential codes generally benefit from as long of a coherence time as possible. Reliability of differential signaling, however, may be further degraded by the presence of carrier frequency offset since the mismatch causes slow phase shifts over time. Doubly differential codes have been proposed to mitigate the effects of the carrier offset [54]. Lastly, many of the receiver structures proposed for differential codes rely on an assumption of Rayleigh fading, restricting the generality of the coding approaches. Motivated by these considerations, we review multi-antenna differential code constructions in the context of reliability and complexity.

An early reintroduction of differential coding in the context of multiple antennas was put forth by Hochwald and Sweldens, who presented constructions inspired by the capacity-achieving construction for the noncoherent MIMO setting in flat Rayleigh fading [37]. Differential codebook design was shown to have a fundamental connection to matrix groups, inspiring the design of a multitude of algebraically constructed differential codes [33, 39, 40, 48, 78]. In a manner similar to unitary space-time code designs, differential codebooks were also designed using maps such as the Cayley Transform to map dispersion matrices to codewords. The decoding approach in [13] reduces the exponential decoding complexity of this approach to a polynomial overhead.

A separate class of MIMO differential codes is based specifically on orthogonal space-time coding structures. Early approaches to differential coding by Jafarkhani and Tarokh built upon generalized orthogonal designs, a special

family of matrices, resulting in differential codes for any number of antennas and an impressive linear decoding complexity in number of antennas and rate [43, 84]. Compared to coherent approaches, however, the rate of these codes appears limited. Rates have been improved for codes leveraging this structure, though it sacrifices the linear decoding complexity [57].

Generally, the bit error rate of differential codes based on space-time code structures incur a performance loss of about 3dB with respect to the bit error rate compared to coherent approaches due to the lack of channel estimates [42]. We confirm the presence of this performance gap in the moderate to high-SNR simulation results presented in Figure (5.2) by comparing the differential approach to the coherent Alamouti space-time code. The gap can be tightened by using larger differential codes spanning over more coherence intervals, but the increase in code size is reflected in the growing receiver complexity [22]. Many proposals for receiver design consider sacrificing optimality in exchange for reducing this exponential overhead [12, 53, 69, 74]. Further results on the bit error performance of multiantenna differential approaches are given in [61, 87].

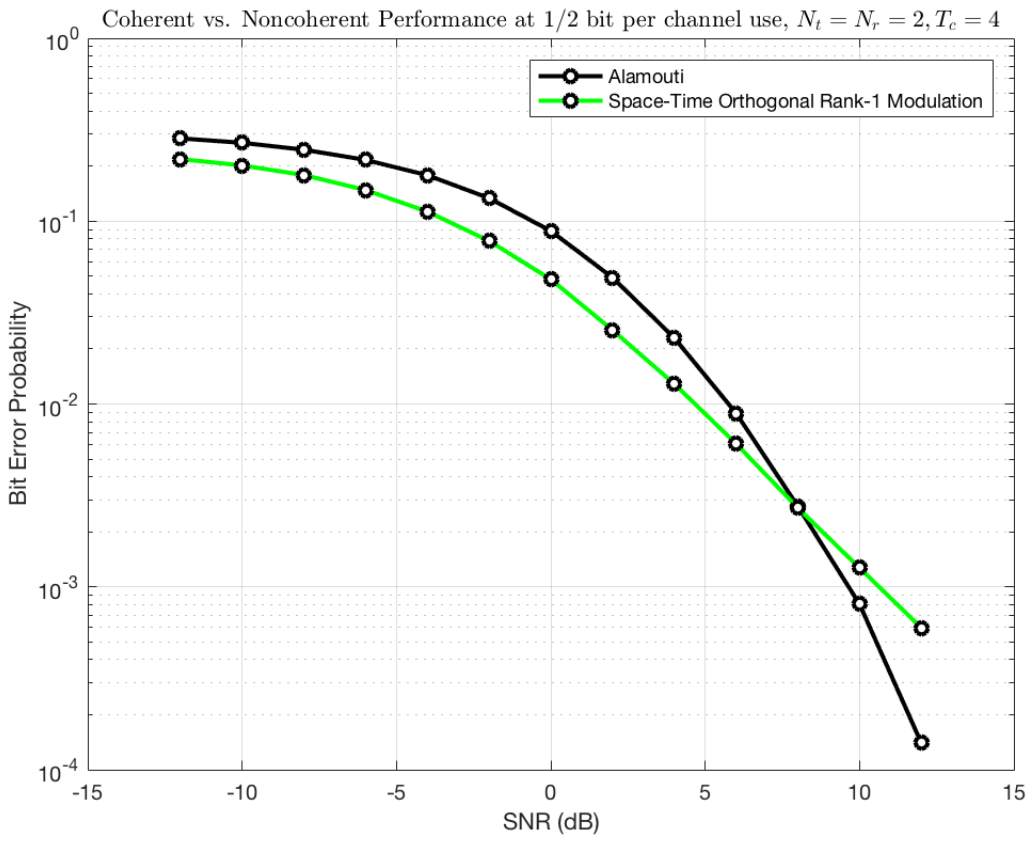

Figure 5.1: Bit error rates for the Alamouti code versus a noncoherent approach at low to moderate SNR. The first approach is the 2×2 Alamouti code with pilot power boosting and least squares channel estimation. For the second approach, we use the noncoherent rank-1 space-time codes designed for low SNR environments (STORM), as reported in [82]. In URLLC, the use of space-time coding can be justified by the fact that for a given target error probability p_e at finite blocklength, the rate that is sacrificed by using diversity in place of maximum multiplexing is negligible given the capacity backoff experienced from the short packet size [18]. The rate is half a bit per channel use.

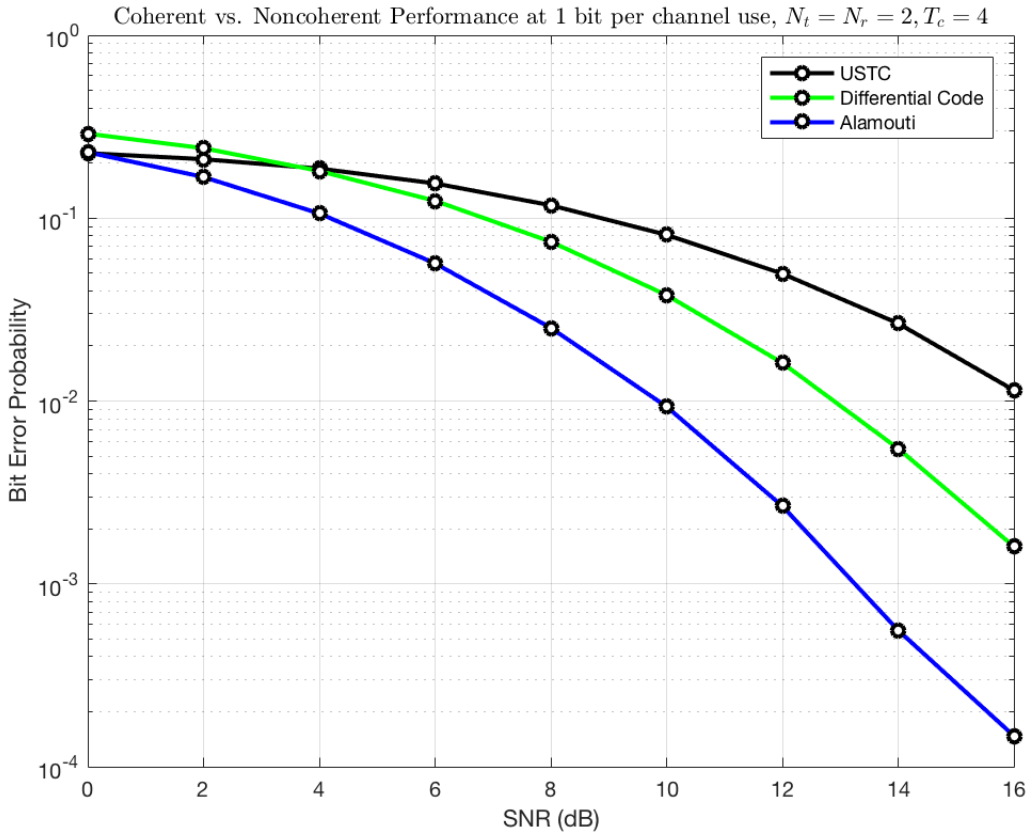

Figure 5.2: Bit error rates for the Alamouti code and two noncoherent approaches at moderate to high SNR. The effects of improved channel estimates become evident at higher SNR, and the Alamouti code gives the best performance. The 3dB gap between the differential code and the Alamouti code observed in [43] is pronounced. USTC is performed using a Grassmannian packing of the appropriate size. This particular packing is not optimized with respect to the product diversity and thus does not perform well.

Chapter 6

Space-Time Code Design

In this section, we present a space-time code construction for the noncoherent MIMO communication environment. The section is based on joint work with Travis Cuvelier and Corey Ostrove appearing in [49]. The approach leverages a Grassmannian packings as the codebook, adapting a quantum error correcting code to map codewords to a space-time code matrix. The design yields a codebook structurally similar to the high-SNR capacity achieving codebook, in the sense that it is a Grassmannian packing. However, while we use both techniques from quantum error correcting codes and Grassmannian packings, our approach to the coding problem is novel. We view the noncoherent channel for a specific MIMO architecture through the lens of quantum errors. We consider the transmitted symbol as a quantum state and design a code to reconstruct that state at the receiver. Our use of Grassmannian frames occurs in a completely different dimension than in [8] and [97] and is derived from the problem of finding quantum states that are maximally separated with respect to the fidelity metric.

Portions of this chapter appeared in Lanham, S. Andrew, et al. "A Noncoherent Space-Time Code from Quantum Error Correction." 2019 53rd Annual Conference on Information Sciences and Systems (CISS). IEEE, 2019. Author T.C. Cuvelier contributed the maximum likelihood decoding rule in Rayleigh fading.

6.1 System Model

We consider a specific canonical received signal model for noncoherent wireless communication [58] [97]. The system has $N_{\mathrm{TX}} = N_{\mathrm{RX}} = 2$ antennas at both the transmitter and receiver. We assume a narrowband model with a single-tap MIMO channel $\mathbf{H} \in \mathbb{C}^{2\times 2}$. We assume a channel coherence time of $T = 4$ channel uses. The transmitted, received, and additive noise signals are denoted by the complex 2×4 matrices $\mathbf{T}$, $\mathbf{Y}$, and $\mathbf{N}$, respectively, where the columns correspond to the time instants in the the coherence interval. We take $\mathbf{N}$ to be a complex Gaussian random matrix with independent, identically distributed entries such that $[\mathbf{N}]_{i,j} \sim \mathcal{N}_{\mathrm{C}}(0, \sigma_n^2)$. We initially assume a Rayleigh fading model where the entries of $\mathbf{H}$ are independent and identically distributed with $[\mathbf{H}]_{i,j} \sim \mathcal{N}_{\mathrm{C}}(0, 1)$. Finally, we assume that $\mathbf{H}$ is constant over the coherence interval but that the channel realizations at different coherence intervals are independent. This model would be most appropriate for a frequency hopping system in an environment with rich scattering. The received signal over the coherence interval is now given by

$$\mathbf{Y} = \mathbf{H}\mathbf{T} + \mathbf{N}. \tag{6.1}$$

Using the standard vectorization identity, letting $\mathbf{y} = \mathrm{vec}(\mathbf{Y})$, $\mathbf{t} = \mathrm{vec}(\mathbf{T})$, $\mathbf{n} = \mathrm{vec}(\mathbf{N})$, and $\overline{\mathbf{H}} = \mathbf{I} \otimes \mathbf{I} \otimes \mathbf{H}$ we can write (6.1) as

$$\mathbf{y} = \overline{\mathbf{H}}\mathbf{t} + \mathbf{n}\ . \tag{6.2}$$

This particular form of the channel model is amenable to the design of a stabilizer code. We now motivate the the application of quantum error correcting

codes in this setting by observing that the communication channel at infinite SNR can be decomposed into a linear combination of Pauli group elements.

The vectorized channel matrix $\overline{\overline{\mathbf{H}}}$ highlights the coherence of the channel coefficients over time and admits a basis decomposition in the Pauli basis $\mathcal{P}_3$ of the form

$$\begin{aligned}\overline{\overline{\mathbf{H}}} &= \mathbf{I} \otimes \mathbf{I} \otimes (c_0\mathbf{I} + c_1\mathbf{X} + c_2\mathbf{Z} + c_3\mathbf{Y}) \\ &= c_0\mathbf{E}_0 + c_1\mathbf{E}_1 + c_2\mathbf{E}_2 + c_3\mathbf{E}_3\end{aligned} \tag{6.3}$$

where

$$c_0 = ([\mathbf{H}]_{1,1} + [\mathbf{H}]_{2,2})/2 \tag{6.4a}$$

$$c_1 = ([\mathbf{H}]_{1,2} + [\mathbf{H}]_{2,1})/2 \tag{6.4b}$$

$$c_2 = ([\mathbf{H}]_{1,1} - [\mathbf{H}]_{2,2})/2 \tag{6.4c}$$

$$c_3 = j([\mathbf{H}]_{1,2} - [\mathbf{H}]_{2,1})/2 \tag{6.4d}$$

and $\mathbf{E}_0 = \mathbf{I} \otimes \mathbf{I} \otimes \mathbf{I}$, $\mathbf{E}_1 = \mathbf{I} \otimes \mathbf{I} \otimes \mathbf{X}$, $\mathbf{E}_2 = \mathbf{I} \otimes \mathbf{I} \otimes \mathbf{Z}$, $\mathbf{E}_3 = \mathbf{I} \otimes \mathbf{I} \otimes \mathbf{Y}$. Defining $\mathbf{c} = [c_0, c_1, c_2, c_3]^T$ we have $\mathbf{c} \sim \mathcal{N}_C(0, \mathbf{I}_4/2)$. The error operators characterizing this channel form the set $E = \{\mathbf{E}_0, \mathbf{E}_1, \mathbf{E}_2, \mathbf{E}_3\}$. This process is analogous to the quantum concept of channel discretization, in which a channel with a continuous set of possible realizations is equivalent to one that randomly applies a discrete set of error operators.

6.2 Code Construction

We now form a stabilizer group satisfying the required conditions for correcting errors introduced by operators in this set. The operators $\mathbf{S}_0 =$

$\mathbf{X} \otimes \mathbf{Z} \otimes \mathbf{X}$ and $\mathbf{S}_1 = \mathbf{X} \otimes \mathbf{X} \otimes \mathbf{Z}$ satisfy the necessary commutation relations to form a set of stabilizer generators, as summarized in Table 6.2.

Commutation Relationships		
	$\mathbf{S}_0$	$\mathbf{S}_1$
$\mathbf{E}_0$	C	C
$\mathbf{E}_1$	C	A
$\mathbf{E}_2$	A	C
$\mathbf{E}_3$	A	A

Table 6.1: Summary of commutation relations between stabilizer and error operators. C denotes commutation and A denotes anti-commutation

Because they commute, the stabilizer operators admit a partially intersecting +1 eigenspace, which has a two-dimensional basis spanned by the vectors

$$\mathbf{v}_0 = \begin{bmatrix} 1 & 0 & 0 & -1 & 0 & 1 & 1 & 0 \end{bmatrix}^T \tag{6.5a}$$

$$\mathbf{v}_1 = \begin{bmatrix} 0 & -1 & -1 & 0 & -1 & 0 & 0 & 1 \end{bmatrix}^T \tag{6.5b}$$

We use these vectors to form a mapping that encodes two arbitrary complex numbers into a space-time code word. Given a complex vector $\mathbf{s} = [s_1,\ s_2]^T$ from a general codebook, we produce the vectorized space-time codeword by applying an encoding operator $\mathbf{C} = \begin{bmatrix} \mathbf{v}_0, & \mathbf{v}_1 \end{bmatrix} \in \mathbb{C}^{8\times 2}$ giving

$$\mathbf{t} = \mathbf{C}\mathbf{s}. \tag{6.6}$$

We assume that the symbol energy is normalized, i.e. $\mathbf{s}^*\mathbf{s} = 1$. This assumption coupled with the definition of $\mathbf{C}$ guarantees that $\mathbf{t}^*\mathbf{t} = 4$ which gives an

average power of unity over the coherence interval. The corresponding 2×4 code matrix for a codeword can be represented with the inverse vectorization operator $\mathrm{vec}^{-1} : \mathbb{C}^8 \mapsto \mathbb{C}^{2\times 4}$,

$$\mathbf{T} = \mathrm{vec}^{-1}(\mathbf{Cs}), \tag{6.7}$$

or

$$\mathbf{T} = \begin{bmatrix} s_1 & -s_2 & -s_2 & s_1 \\ -s_2 & -s_1 & s_1 & s_2 \end{bmatrix}.$$

This code is a *generalized complex orthogonal design* and provides full diversity [42].

The symbol vector $\mathbf{s}$ can be viewed as an information carrying qubit, which we wish to preserve via the stabilizer encoding. Using the interpretation of a qubit as a 1-dimensional subspace of $\mathbb{C}^2$, we assume that symbol vectors $\mathbf{s}$ are drawn uniformly from a constellation $\mathcal{C}$. We choose our constellations as Grassmannian line packings in $\mathbb{C}^2$ [83]. This choice is motivated in the following sections.

6.3 Decoding in Rayleigh Fading Channels

In this setting of quantum-inspired classical coding, we can dispense with the ideas of quantum measurement and syndrome decoding in favor of the more familiar method of maximum likelihood (ML) inference. While our decoding process is based on computing the ML rule, it does lend itself to a quantum mechanical interpretation.

If we assume the encoded symbol $\mathbf{s}$ is drawn uniformly from some constellation $\mathcal{C}$, the maximum a posteriori rule reduces to the canonical ML problem of finding $\hat{\mathbf{s}}$ such that

$$\hat{\mathbf{s}} = \arg\max_{\mathbf{s}\in\mathcal{C}} f_{\mathbf{s}|\mathbf{y}}(\mathbf{s}|\mathbf{y}) = \arg\max_{\mathbf{s}\in\mathcal{C}} f_{\mathbf{y}|\mathbf{s}}(\mathbf{y}|\mathbf{s}) \ . \tag{6.8}$$

We begin by defining the following projection operators:

$$\mathbf{P}_0 = (\mathbf{I}+\mathbf{S}_0)(\mathbf{I}+\mathbf{S}_1)/4 \tag{6.9a}$$

$$\mathbf{P}_1 = (\mathbf{I}+\mathbf{S}_0)(\mathbf{I}-\mathbf{S}_1)/4 \tag{6.9b}$$

$$\mathbf{P}_2 = (\mathbf{I}-\mathbf{S}_0)(\mathbf{I}+\mathbf{S}_1)/4 \tag{6.9c}$$

$$\mathbf{P}_3 = (\mathbf{I}-\mathbf{S}_0)(\mathbf{I}-\mathbf{S}_1)/4 \ . \tag{6.9d}$$

Note that $\mathbf{P}_0$ is the projector onto the code space and $\mathbf{P}_0+\mathbf{P}_1+\mathbf{P}_2+\mathbf{P}_3 = \mathbf{I}$ is the identity. The receiver computes the four corresponding projections of the received vector $\mathbf{y}$ onto the code space and the three error subspaces to obtain

$$\mathbf{P}_0\mathbf{y} = c_0\mathbf{t} + \mathbf{P}_0\mathbf{n} \tag{6.10a}$$

$$\mathbf{P}_1\mathbf{y} = c_1\mathbf{E}_1\mathbf{t} + \mathbf{P}_1\mathbf{n} \tag{6.10b}$$

$$\mathbf{P}_2\mathbf{y} = c_2\mathbf{E}_2\mathbf{t} + \mathbf{P}_2\mathbf{n} \tag{6.10c}$$

$$\mathbf{P}_3\mathbf{y} = c_3\mathbf{E}_3\mathbf{t} + \mathbf{P}_3\mathbf{n} \ , \tag{6.10d}$$

where the c_0, c_1, c_2, and c_3 are as defined in (6.4) and we have used the fact that $\mathbf{P}_k\mathbf{E}_k = \mathbf{E}_k\mathbf{P}_0$. Since the projectors in (6.9) sum to identity, the vectors in (6.10) are sufficient statistics for $\mathbf{y}$. Recall that $\mathbf{c} = [c_0, c_1, c_2, c_3]^T \sim \mathcal{N}_{\mathrm{C}}(\mathbf{0}, \mathbf{I}/2)$ and is independent of the noise.

The receiver now carriers out error correction on the projected vectors. The receiver applies a unitary correction operator $\mathbf{E}_k$ to each projection $\mathbf{P}_k\mathbf{y}$ and obtains

$$\mathbf{z}_0 = c_0\mathbf{t} + \mathbf{n} \tag{6.11a}$$

$$\mathbf{z}_1 = c_1\mathbf{t} + \mathbf{E}_1\mathbf{P}_1\mathbf{n} \tag{6.11b}$$

$$\mathbf{z}_2 = c_2\mathbf{t} + \mathbf{E}_2\mathbf{P}_2\mathbf{n} \tag{6.11c}$$

$$\mathbf{z}_3 = c_3\mathbf{t} + \mathbf{E}_3\mathbf{P}_3\mathbf{n}\ . \tag{6.11d}$$

Since the $\mathbf{P}_k$ are orthogonal projection operators, the projected and corrected noise vectors, $\mathbf{E}_k\mathbf{P}_k\mathbf{n}$, are mutually independent. Following from this, the commutation relationships and unitarity of the correction operators imply that the resulting noise vectors are identically distributed with $\mathbf{E}_k\mathbf{P}_k\mathbf{n} \sim \mathcal{N}_{\mathrm{C}}(0, \sigma_n^2\mathbf{P}_0)$ for all k. Since $\mathbf{t} = \mathbf{C}\mathbf{s}$, projections of the $\mathbf{z}_k$ onto the column space of $\mathbf{C}$ are sufficient to estimate $\mathbf{s}$. Letting $\mathbf{n}_k = \mathbf{C}^*\mathbf{E}_k\mathbf{P}_k\mathbf{n}/(2\sqrt{2})$, and letting $\hat{c}_k = \sqrt{2}c_k$ the receiver computes

$$\mathbf{q}_k = \frac{\mathbf{C}^*\mathbf{z}_k}{2\sqrt{2}} = \hat{c}_k\mathbf{s} + \mathbf{n}_k\ ,\ \text{for } k \in \{0,1,2,3\}\ . \tag{6.12}$$

The $\mathbf{n}_k$ are independent and identically distributed with $\mathbf{n}_k \sim \mathcal{N}_{\mathrm{C}}(\mathbf{0}, \sigma_n^2\mathbf{I}/2)$. The scaled-identity covariance follows from the fact that $\mathbf{P}_0\mathbf{C} = \mathbf{C}$, since the columns of $\mathbf{C}$ are by definition in the code, and that $\mathbf{C}^*\mathbf{C} \propto \mathbf{I}$.

We now concatenate the $\mathbf{q}_k$ into the vector $\mathbf{q} = [\mathbf{q}_0^T, \mathbf{q}_1^T, \mathbf{q}_2^T, \mathbf{q}_3^T]^T$ and reformulate our maximum likelihood problem as

$$\hat{\mathbf{s}} = \arg\max_{\mathbf{s}} f_{\mathbf{q}|\mathbf{s}}(\mathbf{q}|\mathbf{s}). \tag{6.13}$$

Given the transmit symbol $\mathbf{s}$, $\mathbf{q}$ is a Gaussian random vector. We define $\mathbf{w} = [\hat{\mathbf{c}}^T, \mathbf{n}_0^T, \mathbf{n}_1^T, \mathbf{n}_2^T, \mathbf{n}_3^T]^T$ so that $\mathbf{w} \sim \mathcal{N}_{\mathrm{C}}(\mathbf{0}, \mathbf{\Sigma})$, where

$$\mathbf{\Sigma} = \begin{bmatrix} \mathbf{I}_4 & \mathbf{0}_{4\times 8} \\ \mathbf{0}_{8\times 4} & \frac{\sigma_n^2}{2}\mathbf{I}_8 \end{bmatrix}. \tag{6.14}$$

Defining the matrix $\mathbf{M} \in \mathbb{C}^{8\times 12}$ via

$$\mathbf{M} = \begin{bmatrix} (\mathbf{I}_4 \otimes \mathbf{s}) & \mathbf{I}_8 \end{bmatrix}, \tag{6.15}$$

we have

$$\mathbf{q} = \mathbf{M}\mathbf{w}. \tag{6.16}$$

Thus, $\mathbf{q} \sim \mathcal{N}_{\mathrm{C}}(\mathbf{0}, \mathbf{Q})$, where $\mathbf{Q} = \mathbf{M}\mathbf{\Sigma}\mathbf{M}^*$. It can be shown that

$$\mathbf{Q} = \mathbf{I}_4 \otimes \left(\mathbf{s}\mathbf{s}^* + \frac{\sigma_n^2}{2}\mathbf{I}_{2\times 2} \right). \tag{6.17}$$

It turns out that the second definition of $\mathbf{Q}$ is useful in simplifying the likelihood function.

Assuming that $\mathbf{Q}$ is invertible, the likelihood function can be written as

$$f_{\mathbf{q}|\mathbf{s}}(\mathbf{q}|\mathbf{s}) = \frac{\exp(-\mathbf{q}^*\mathbf{Q}^{-1}\mathbf{q})}{\pi^8 \det(\mathbf{Q})}. \tag{6.18}$$

Using the property of determinants of Kronecker products yields $\det(\mathbf{Q}) = \det(\mathbf{s}\mathbf{s}^* + \frac{\sigma_n^2}{2}\mathbf{I}_{2\times 2})^4$. Since, by assumption $\mathbf{s}^*\mathbf{s} = 1$, we have $\det(\mathbf{Q}) = [(1 + \frac{\sigma_n^2}{2})\frac{\sigma_n^2}{2}]^4$, which is constant in $\mathbf{s}$. Furthermore, using the Kronecker product

definition it is clear that $\mathbf{Q}^{-1} = \mathbf{I}_{4\times 4} \otimes (\mathbf{s}\mathbf{s}^* + \frac{\sigma_n^2}{2}\mathbf{I}_{2\times 2})^{-1}$. Designating $\mathbf{U}_\mathbf{s} = (\mathbf{s}\mathbf{s}^* + \frac{\sigma_n^2}{2}\mathbf{I}_{2\times 2})^{-1}$ and calculating the inverse explicitly yields

$$\mathbf{U}_\mathbf{s} = \frac{1}{\frac{\sigma_n^2}{2}(1+\frac{\sigma_n^2}{2})} \begin{bmatrix} |s_2|^2 + \frac{\sigma_n^2}{2} & -s_1 s_2^* \\ -s_2 s_1^* & |s_1|^2 + \frac{\sigma_n^2}{2} \end{bmatrix}, \tag{6.19}$$

which allows us to (finally) write down an explicit decision rule. Substituting (6.18) into (6.13) and using the simplifications in (6.19) and the preceding paragraph motivate the decision rule

$$\hat{\mathbf{s}} = \arg\min_{\mathbf{s}\in\mathcal{C}} \mathbf{q}^*(\mathbf{I}_{4\times 4} \otimes \mathbf{U}_\mathbf{s})\mathbf{q} \, . \tag{6.20}$$

We simplify further by noting that, since $\mathbf{s}$ is normalized,

$$\mathbf{U}_\mathbf{s} \propto \frac{\sigma^2}{2}\mathbf{I}_2 + (\mathbf{I}_2 - \mathbf{s}\mathbf{s}^*) \, . \tag{6.21}$$

Thus, using (6.21), (6.20) can be written

$$\hat{\mathbf{s}} = \arg\max_{\mathbf{s}\in\mathcal{C}} \sum_{k=0}^{3} \mathbf{q}_k^* \mathbf{s}\mathbf{s}^* \mathbf{q}_k = \arg\max_{\mathbf{s}\in\mathcal{C}} \mathbf{s}^* \sum_{k=0}^{3} (\mathbf{q}_k \mathbf{q}_k^*)\mathbf{s} \, . \tag{6.22}$$

This form of the decoding rule lends itself to a quantum mechanical interpretation. We interpret $\hat{\mathbf{q}}_k\hat{\mathbf{q}}_k^* = \mathbf{q}_k\mathbf{q}_k^*/\mathrm{tr}(\mathbf{q}_k\mathbf{q}_k^*)$ as normalized density operators. We consider the mixed state, $\mathbf{\Psi}$ formed from drawing the states $\hat{\mathbf{q}}_k\hat{\mathbf{q}}_k^*$ with respective probabilities

$$p_k = \frac{\mathrm{tr}(\mathbf{q}_k\mathbf{q}_k^*)}{\sum_{i=0}^{3} \mathrm{tr}(\mathbf{q}_i\mathbf{q}_i^*)} \, . \tag{6.23}$$

This yields the density matrix

$$\mathbf{\Psi} = \frac{\sum_{i=0}^{3} \mathbf{q}_i \mathbf{q}_i^*}{\sum_{i=0}^{3} \mathrm{tr}(\mathbf{q}_i \mathbf{q}_i^*)}, \tag{6.24}$$

which is the same matrix that appears on the right hand side of (6.22) up to a positive scale factor. Thus, using the definition of fidelity (cf. 2.1) it can be seen that the ML detection rule consists of finding the input state that maximizes the fidelity with respect to $\mathbf{\Psi}$, or, more explicitly,

$$\hat{\mathbf{s}} = \arg\max_{\mathbf{s}\in\mathcal{C}} F(\mathbf{\Psi}, \mathbf{s}\mathbf{s}^*). \tag{6.25}$$

We used the fact that maximizing the fidelity is the same as maximizing its square. We discuss our choice of constellation set $\mathcal{C}$ in the following section.

6.3.1 Qubit Symbol Constellation

The detection rule in (6.22) motivates our choice of the Grassmannian frame for our qubit constellation. Consider the expectation

$$\mathbf{B} = \mathbb{E}\left[\sum_{k=0}^{3} \mathbf{q}_k \mathbf{q}_k^* \mid \mathbf{s}\right] = 4\mathbf{s}\mathbf{s}^* + 2\sigma_n^2 \mathbf{I}_2 \tag{6.26}$$

and consider the function $R_{\mathbf{s}}(\hat{\mathbf{s}}) = \mathbf{s}\mathbf{B}\mathbf{s}^* - \hat{\mathbf{s}}\mathbf{B}\hat{\mathbf{s}}^*$, where $\mathbf{s} \neq \hat{\mathbf{s}}$. This is the expected value of the difference between computing the statistic in (6.22) on the transmitted symbol as opposed to another, not transmitted symbol. We expect that the dominant error will occur when $R_{\mathbf{s}}(\hat{\mathbf{s}})$ is minimized over all $\mathbf{s}$ and $\hat{\mathbf{s}}$. We therefore seek a constellation set with the maximal minimum $R_{\mathbf{s}}(\hat{\mathbf{s}})$.

Since the transmit symbols are normalized, the definition of $R_{\mathbf{s}}(\hat{\mathbf{s}})$ indicates that for a N-point constellation encoding $\log_2(N)$ bits we should select the set given by

$$\hat{\mathcal{C}} = \min_{\mathcal{C}=\{\mathbf{s}\in\mathbb{C}^2|\mathbf{s}^*\mathbf{s}=1\},|\mathcal{C}|=N} \max |\hat{\mathbf{s}}^*\mathbf{s}|^2 \tag{6.27}$$

This indicates that we should choose our constellation as a Grassmanian packing [83] [56]. Furthermore, in the quantum picture, this is akin to choosing input states that are maximally far apart with respect to a metric induced by fidelity.

6.4 Decoding in Ricean Fading Channels

In some communication settings, one or more of the multipath terms dominate the received signal, typically due to the presence of a line-of-sight path between transmitter and receiver. This scenario is captured by the Ricean fading model, where the MIMO channel matrix $\mathbf{H}$ can be decomposed into the sum of a deterministic line-of-sight channel matrix $\mathbf{H}_{\mathsf{LOS}}$ and a scattering matrix $\mathbf{H}_{\mathsf{w}}$ with $\mathcal{N}_C(0,1)$ distributed entries [34]. The Rice factor K determines the prevalence of each of these components, giving the channel model

$$\mathbf{H} = \sqrt{\frac{\mathsf{K}}{1+\mathsf{K}}}\mathbf{H}_{\mathsf{LOS}} + \sqrt{\frac{1}{1+\mathsf{K}}}\mathbf{H}_{\mathsf{w}}. \tag{6.28}$$

Denoting the line-of-sight matrix $\mathbf{H}_{\mathsf{LOS}} = \boldsymbol{\mu}$, we define a set of terms similar to Equation (6.4) for each component matrix, which will feature in our final

Pauli basis decomposition of $\mathbf{H}$. Those terms are

$$m_0 = ([\boldsymbol{\mu}]_{1,1} + [\boldsymbol{\mu}]_{2,2})/2, \quad w_0 = ([\mathbf{H}_{\mathsf{w}}]_{1,1} + [\mathbf{H}_{\mathsf{w}}]_{2,2})/2 \tag{6.29a}$$

$$m_1 = ([\boldsymbol{\mu}]_{1,2} + [\boldsymbol{\mu}]_{2,1})/2, \quad w_1 = ([\mathbf{H}_{\mathsf{w}}]_{1,1} + [\mathbf{H}_{\mathsf{w}}]_{2,2})/2 \tag{6.29b}$$

$$m_2 = ([\boldsymbol{\mu}]_{1,1} - [\boldsymbol{\mu}]_{2,2})/2, \quad w_2 = ([\mathbf{H}_{\mathsf{w}}]_{1,1} + [\mathbf{H}_{\mathsf{w}}]_{2,2})/2 \tag{6.29c}$$

$$m_3 = j([\boldsymbol{\mu}]_{1,2} - [\boldsymbol{\mu}]_{2,1})/2, \quad w_3 = j([\mathbf{H}_{\mathsf{w}}]_{1,1} + [\mathbf{H}_{\mathsf{w}}]_{2,2})/2. \tag{6.29d}$$

Assimilating constant factors into $g_{\mathsf{LOS}} = \frac{1}{2}\sqrt{\frac{\mathsf{K}}{1+\mathsf{K}}}$ and $g_{\mathsf{w}} = \frac{1}{2}\sqrt{\frac{1}{1+\mathsf{K}}}$, , we let $c_i = g_{\mathsf{LOS}} m_i + g_{\mathsf{w}} w_i$ for $i = 0, \ldots, 3$. The Pauli basis decomposition of the vectorized equivalent Ricean channel model is given as

$$\overline{\mathbf{H}} = \mathbf{I} \otimes \mathbf{I} \otimes (c_0\mathbf{I} + c_1\mathbf{X} + c_2\mathbf{Z} + c_3\mathbf{Y}). \tag{6.30}$$

As expected, the error operators remain identical to those characterizing the Rayleigh fading model, $E = \{\mathbf{E}_0, \mathbf{E}_1, \mathbf{E}_2, \mathbf{E}_3\}$, indicating the compatibility of our stabilizer code construction for the Ricean fading setting. However, the distribution of the scalar constants changes, which will modify the maximum-likelihood decoding rule. We aggregate the variables c_i, m_i, and w_i into the vectors $\mathbf{c}, \mathbf{m}, \mathbf{w}$, which satisfy $\mathbf{c} = \mathbf{m} + \mathbf{w}$. We observe that $\mathbf{c} \sim \mathcal{N}_C(g_{\mathsf{LOS}}\mathbf{m}, g_{\mathsf{w}}^2\mathbf{I}_4)$.

Because the code construction for the Ricean fading setting is identical to that of Rayleigh fading, we begin from the reformulated maximum likelihood problem given in Equation (6.13), which uses the decoded symbol vectors to compute the most likely received data. Letting $\hat{\mathbf{c}} = \sqrt{2}\mathbf{c}$ and $\mathbf{n}_k$ as before, we observe that the mean of $\mathbf{w} = [\hat{\mathbf{c}}, \mathbf{n}_0, \mathbf{n}_1, \mathbf{n}_2, \mathbf{n}_3]$ has changed such that $\mathbf{w} \sim \mathcal{N}_C(\boldsymbol{\mu}_{\mathbf{w}}, \boldsymbol{\Sigma})$ where

$$\boldsymbol{\mu}_{\mathbf{w}} = \begin{bmatrix} g_{\mathsf{LOS}}\mathbf{m} \\ \mathbf{0}_{8\times 1} \end{bmatrix} \tag{6.31}$$

The covariance matrix $\mathbf{\Sigma}$ in turn becomes

$$\mathbf{\Sigma} = \begin{bmatrix} g_{\mathsf{w}}^2 \mathbf{I}_4 & \mathbf{0}_{4\times 8} \\ \mathbf{0}_{8\times 4} & \frac{\sigma_n^2}{2}\mathbf{I}_8 \end{bmatrix} \tag{6.32}$$

Letting $\mathbf{q} = \mathbf{M}\mathbf{w}$ with $\mathbf{M}$ defined as in Equation (6.15) and $\mathbf{Q} = \mathbf{M}\mathbf{\Sigma}\mathbf{M}^*$, we have $\mathbf{q} \sim \mathcal{N}_C(\boldsymbol{\mu}_{\mathbf{w}}, \mathbf{Q})$, and the new likelihood function tailored to Ricean fading is given as

$$f_{\mathbf{q}|\mathbf{s}}(\mathbf{q}|\mathbf{s}) = \frac{\exp\left(-(\mathbf{q}-\boldsymbol{\mu}_{\mathbf{w}})\mathbf{Q}^{-1}(\mathbf{q}-\boldsymbol{\mu}_{\mathbf{w}})\right)}{\pi^8 \det(\mathbf{Q})} \tag{6.33}$$

We see that the Ricean line-of-sight matrix manifests as a non-zero mean adjustment in the likelihood maximization problem, while the Rice factor manifests in both of the statistics of $\mathbf{q}$. Carrying through the minimization yields a slight modification to the rule proposed for Rayleigh fading in Equation (6.22), namely, letting $\mathbf{m}_k = [m_k, m_k]^T$ for $k = \{0, \ldots, 3\}$,

$$\hat{\mathbf{s}} = \arg\max_{s\in\mathcal{C}} \mathbf{s}^* \sum_{k=0}^{3} \left(\mathbf{q}_k - g_{\mathsf{LOS}}\mathbf{m}_k\right)\left(\mathbf{q}_k - g_{\mathsf{LOS}}\mathbf{m}_k\right)^* \mathbf{s}. \tag{6.34}$$

In this context, the maximum likelihood problem can be viewed as a computation maximizing the fidelity between a candidate input symbol and a mixed state comprised of mean-adjusted received symbols $(\mathbf{q}_k - g_{\mathsf{LOS}}\mathbf{m}_k)$. This presence of the mean does not change the considerations of Section 6.3.1, and we can continue to choose symbols that form a Grassmannian packing.

6.5 Simulation Results and Conclusions

In this section, we present simulation results to demonstrate the performance of the noncoherent space-time code presented in Section 6.3. We

have considered Grassmannian packings of size $N = 4$ and $N = 8$ in $\mathbb{C}^2$ with a Rayleigh fading environment. Specifically, we used the Grassmanian packings listed on [55].

We compare the stabilizer-based, non-coherent construction with a coherent scheme based on the Alamouti code (for 2×2 systems) at spectral efficiency rates of $r = 1/2$ and $r = 1$ bits/channel use [6]. Channel estimation is first performed by transmitting the symbols $[1, 1]^T/\sqrt{2}$ and $[1, -1]^T/\sqrt{2}$ and solving for an estimate of $\mathbf{H}$ at the receiver. We then use the Alamouti scheme to transmit one space time symbol $\mathbf{s} \in \mathbb{C}^2$ over the remaining two channel uses in the coherence interval. We encode in $\mathbf{s}$ two binary phase-shift keying (BPSK) symbols for the rate $r = 1/2$ approach and two quadrature phase-shift keying (QPSK) symbols for the rate $r = 1$ approach.

Similarly, we compare to an approach using differential unitary group codes, as outlined in [39]. At both $r = 1/2$ and $r = 1$, the first two channel uses are used for the 2×2 reference matrix, and no information is transmitted. With the next two channel uses we transmit a single differentially encoded 2×2 matrix drawn from an appropriately sized constellation. For $r = 1/2$, this constellation is a group code over the QPSK constellation; specifically, we encode over the 2×2 Pauli group elements. For $r = 1$, this constellation is a dicylic group code generated over 16-PSK. The transmit symbols in both sets of comparisons are appropriately normalized so that the transmit power is constant over the four transmissions.

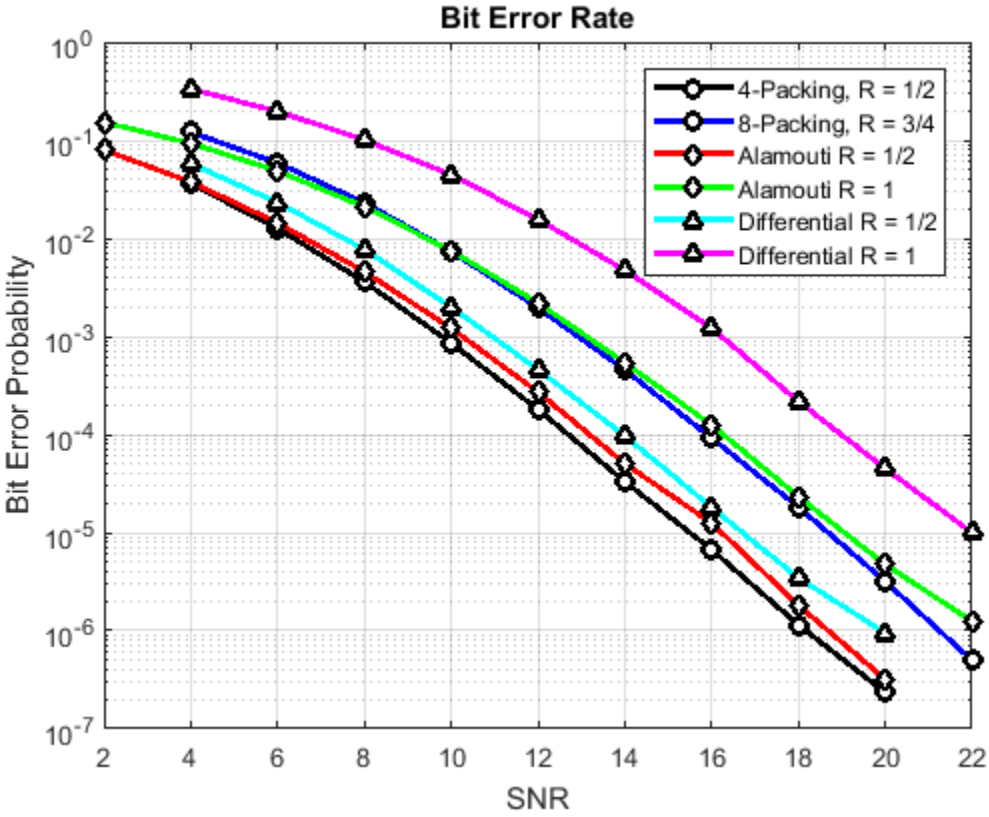

Figure 6.1: Bit error rate for various packings. We simulated 10 million channel realizations (assumed to be coherent for four instances each). For SNRs with bit error rates lower than 10^{-6}, we simulated 100 million channel realizations.

Chapter 7

Conclusion

In this thesis, we have proposed applications of quantum information processing methods to classical systems. The mathematical similarity between quantum mechanical systems and certain classical systems presents the opportunity to modify and apply processing based on quantum error correction and gate-based quantum computing to demonstrate advantageous performance in classical systems. The advantage can arise by leveraging properties of classical systems to accurately emulate quantum information, as in the case of the quantum emulation device, or it can arise from treating classical information in a manner similar to quantum information, as in the case of the space-time code design.

This invites a further analysis of the relationship between classical information and quantum information, as well as a look at the properties of the physical systems used to encode such information. In our construction of the quantum emulation device, we created an analog system capable of representing and processing normalized state vectors for multi-qubit systems. More work is needed to understand the key limitations in using such a classical system to process emulated quantum states, and how these limitations

arise. For example, the noise characteristics of a classical analog system are significantly different from those of a quantum system. Scalability of such systems is also an important concern, as the dimension of a quantum state space scales exponentially in the number of qubits. Nevertheless, there may exist intermediate-scale settings or environments in which it is advantageous to use analog signals instead of quantum systems to process information. It will be important to identify such regimes and explore the possibility of using system design concepts from the mature analog signal processing industry to improve computational performance.

This thesis also presented an adaptation of a quantum error correcting code for the noncoherent wireless mobile communication setting with competitive bit error rates. This gives some insight into the interplay between quantum information preservation methods and wireless communication protocols that operate with only statistical channel characterizations rather than instantaneous channel knowledge. The space-time code exhibits many desirable properties in wireless communication, such as full diversity and robust performance in a variety of statistical channel models. It also has an encoding structure resemblant to a Grassmannian signaling scheme, a capacity-achieving approach in noncoherent environments. Future work is needed to extend the code into a family of designs for different multiantenna system configurations and to analyze the resultant performance across channel parameters discussed in Chapter 4, such as block-length and coherence time, with further simulations to confirm the performance. Work is also needed to analyze the code with re-

spect to new results in finite-blocklength information theory with applications to emerging demands for low-latency and highly reliable communication.

Bibliography

[1] Technical specification group radio access network; evolved universal terrestrial radio access (E-UTRA); multiplexing and channel coding (release 10). document TS 36.212, 3GPP, December 2012. [Online]. Available: http://www.3gpp.org/.

[2] Requirements for further advancements for evolved universal terrestrial radio access (E-UTRA) (LTE-Advanced) (release 15). Document TR 36.913, 3GPP, 2014. [Online]. Available: http://www.3gpp.org/DynaReport/36913.htm.

[3] Study on New Radio (NR) Access Technology Physical Layer Aspects. document TR 38.802 v14.2, 3GPP, March 2017.

[4] I. Abou-Faycal, M. Trott, and S. Shamai. The capacity of discrete-time memoryless rayleigh-fading channels. *IEEE Transactions on Information Theory*, 47(4):1290–1301, May 2001.

[5] D. Agrawal, T. Richardson, and R. Urbanke. Multiple-antenna signal constellations for fading channels. *IEEE Transactions on Information Theory*, 47(6):2618–2626, 2001.

[6] S. Alamouti. A simple transmit diversity technique for wireless communications. *IEEE Journal on Selected Areas in Communication*, 16(8):1451–

1458, Oct 1998.

[7] A. Ashikhmin and R. Calderbank. Space-time Reed-Muller codes for noncoherent MIMO transmission. In *Proceedings of the International Symposium on Information Theory*, pages 1952–1956. IEEE, 2005.

[8] A. Ashikhmin and R. Calderbank. Grassmannian packings from operator Reed-Muller codes. *IEEE Transactions on Information Theory*, 56(11):5689–5714, 2010.

[9] M. Beko, J. Xavier, and V. Barroso. Further results on the capacity and error probability analysis of noncoherent MIMO systems in the low SNR regime. *IEEE Transactions on Signal Processing*, 56(7):2915–2930, 2008.

[10] C. Bockelmann, N. Pratas, H. Nikopour, K. Au, T. Svensson, C. Stefanovic, P. Popovski, and A. Dekorsy. Massive machine-type communications in 5G: Physical and MAC-layer solutions. *IEEE Communications Magazine*, 54(9):59–65, 2016.

[11] M. Borran, A. Sabharwal, and B. Aazhang. On design criteria and construction of noncoherent space-time constellations. *IEEE Transactions on Information Theory*, 49(10):2332–2351, 2003.

[12] E. Chiavaccini and G. Vitetta. Further results on differential space-time modulations. *IEEE Transactions on Communications*, 51(7):1093–1101, 2003.

[13] K. Clarkson, W. Sweldens, and A. Zheng. Fast multiple-antenna differential decoding. *IEEE Transactions on Communications*, 49(2):253–261, 2001.

[14] G. Colman, R. Gohary, M. El-Azizy, T. Willink, and T. Davidson. Quasi-gray labelling for grassmannian constellations. *IEEE Transactions on Wireless Communications*, 10(2):626–636, 2011.

[15] S. de la Kethulle de Ryhove, N. Marina, and G. Oien. On the mutual information and low-snr capacity of memoryless noncoherent rayleigh-fading channels. *IEEE Transactions on Information Theory*, 54(7):3221–3231, 2008.

[16] D. Deutsch. Quantum theory, the Church–Turing principle and the universal quantum computer. *Proceedings of the Royal Society of London. A. Mathematical and Physical Sciences*, 400(1818):97–117, 1985.

[17] D. Deutsch and R. Jozsa. Rapid solution of problems by quantum computation. *Proceedings of the Royal Society of London. Series A: Mathematical and Physical Sciences*, 439(1907):553–558, 1992.

[18] G. Durisi, T. Koch, J. Östman, Y. Polyanskiy, and W. Yang. Short-packet communications over multiple-antenna rayleigh-fading channels. *IEEE Transactions on Communications*, 64(2):618–629, 2016.

[19] G. Durisi, U. Schuster, H. Bolcskei, and S. Shamai. Noncoherent capacity of underspread fading channels. *IEEE Transactions on Information*

Theory, 56(1):367–395, 2010.

[20] R. Etkin and D. Tse. Degrees of freedom in some underspread MIMO fading channels. *IEEE Transactions on Information Theory*, 52(4):1576–1608, 2006.

[21] P. Fan, E. Panayirci, H. Poor, and P. Mathiopoulos. Special issue on broadband mobile communications at very high speeds. *EURASIP Journal on Wireless Communications and Networking*, 2012(1):279, Aug 2012.

[22] C. Gao, A. Haimovich, and D. Lao. Multiple-symbol differential detection for mpsk space-time block codes: decision metric and performance analysis. *IEEE Transactions on Communications*, 54(8):1502–1510, 2006.

[23] R. Gohary and H. Yanikomeroglu. Noncoherent MIMO signaling for block-fading channels: Approaches and challenges. *IEEE Vehicular Technology Magazine*, 14(1):80–88, 2019.

[24] D. Gottesman. *Stabilizer Codes and Quantum Error Correction*. PhD thesis, The California Institute of Technology, 1997.

[25] L. Grover. A fast quantum mechanical algorithm for database search. *arXiv preprint quant-ph/9605043*, 1996.

[26] M. Gursoy, H. Poor, and S. Verdú. The noncoherent Rician fading channel-part i: structure of the capacity-achieving input. *IEEE Transactions on Wireless Communications*, 4(5):2193–2206, 2005.

[27] M. Gursoy, H. Poor, and S. Verdú. Noncoherent Rician fading channel-part ii: spectral efficiency in the low-power regime. *IEEE Transactions on Wireless Communications*, 4(5):2207–2221, 2005.

[28] M. Gursoy, H. Poor, and S. Verdú. On-off frequency-shift keying for wide-band fading channels. *EURASIP Journal on Wireless Communications and Networking*, 2006(1):098564, 2006.

[29] G. Han and J. Rosenthal. Geometrical and numerical design of structured unitary space–time constellations. *IEEE Transactions on Information Theory*, 52(8):3722–3735, 2006.

[30] T. Harty, D. Allcock, C. Ballance, L. Guidoni, H. Janacek, N. Linke, D. Stacey, and D. Lucas. High-fidelity preparation, gates, memory, and readout of a trapped-ion quantum bit. *Physical Review Letters*, 113(22):220501, 2014.

[31] B. Hassibi and B. Hochwald. Cayley differential unitary space-time codes. *IEEE Transactions on Information Theory*, 48(6):1485–1503, 2002.

[32] B. Hassibi and Y. Jing. Unitary space-time modulation via the cayley transform. In *Proceedings IEEE International Symposium on Information Theory*, page 134. IEEE, 2002.

[33] B. Hassibi and M. Khorrami. Fully-diverse multiple-antenna signal constellations and fixed-point-free lie groups. In *Proceedings IEEE International Symposium on Information Theory*, pages 199–. IEEE, June 2001.

[34] R. Heath Jr. and A. Lozano. *Foundations of MIMO Communication*. Cambridge University Press, 2018.

[35] B. Hochwald and T. Marzetta. Unitary space-time modulation for multiple-antenna communications in rayleigh flat fading. *IEEE Transactions on Information Theory*, 46(2):543–564, 2000.

[36] B. Hochwald, T. Marzetta, W. Sweldens T. Richardson, and R. Urbanke. Systematic design of unitary space-time constellations. *IEEE Transactions on Information Theory*, 46(6):1962–1973, 2000.

[37] B. Hochwald and W. Sweldens. Differential unitary space-time modulation. *IEEE Transactions on Communications*, 48(12):2041–2052, 2000.

[38] J. Huang and S. Meyn. Characterization and computation of optimal distributions for channel coding. *IEEE Transactions on Information Theory*, 51(7):2336–2351, 2005.

[39] B. Hughes. Differential space-time modulation. *IEEE Transactions on Information Theory*, 46(7):2567–2578, Nov 2000.

[40] B. Hughes. Optimal space-time constellations from groups. *IEEE Transactions on Information Theory*, 49(2):401–410, 2003.

[41] I. Jacobs. The asymptotic behavior of incoherent M-ary communication systems. *Proceedings of the IEEE*, 51(1):251–252, Jan 1963.

[42] H. Jafarkhani. *Space-Time Coding: Theory and Practice*. Cambridge University Press, 2005.

[43] H. Jafarkhani and V. Tarokh. Multiple transmit antenna differential detection from generalized orthogonal designs. *IEEE Transactions on Information Theory*, 47(6):2626–2631, 2001.

[44] X. Jin, A. Eckford, and T. Fuja. LDPC codes for non-coherent block fading channels with correlation: analysis and design. *IEEE Transactions on Communications*, 56(1):70–80, January 2008.

[45] M. Johnson, M. Amin, S. Gildert, T. Lanting, F. Hamze, N. Dickson, R. Harris, A. Berkley, J. Johansson, P. Bunyk, et al. Quantum annealing with manufactured spins. *Nature*, 473(7346):194, 2011.

[46] I. Kammoun and J. Belfiore. A new family of Grassmann space-time codes for non-coherent MIMO systems. *IEEE Communications Letters*, 7(11):528–530, 2003.

[47] B. La Cour and G. Ott. Signal-based classical emulation of a universal quantum computer. *New Journal of Physics*, 17(5):053017, 2015.

[48] L. Lampe, R. Schober, and R. Fischer. Coded differential space-time modulation for flat fading channels. *IEEE Transactions on Wireless Communications*, 2(3):582–590, 2003.

[49] S Andrew Lanham, Travis C Cuvelier, Corey Ostrove, Brian La Cour, Granville Ott, and Robert Heath Jr. A noncoherent space-time code

from quantum error correction. In *2019 53rd Annual Conference on Information Sciences and Systems (CISS)*, pages 1–6. IEEE, 2019.

[50] A. Lapidoth and N. Miliou. Duality bounds on the cutoff rate with applications to ricean fading. *IEEE Transactions on Information Theory*, 52(7):3003–3018, 2006.

[51] A. Lapidoth and S. Moser. Capacity bounds via duality with applications to multiple-antenna systems on flat-fading channels. *IEEE Transactions on Information Theory*, 49(10):2426–2467, 2003.

[52] Y. Liang and V. Veeravalli. Capacity of noncoherent time-selective rayleigh-fading channels. *IEEE Transactions on Information Theory*, 50(12):3095–3110, 2004.

[53] C. Ling, K. Li, and A. Kot. Noncoherent sequence detection of differential space-time modulation. *IEEE Transactions on Information Theory*, 49(10):2727–2734, 2003.

[54] Z. Liu, G. Giannakis, and B. Hughes. Double differential space-time block coding for time-selective fading channels. *IEEE Transactions on Communications*, 49(9):1529–1539, 2001.

[55] D. Love. Grassmannian subspace packing. [Online] `https://engineering.purdue.edu/~djlove/grass.html`.

[56] D. Love and R. Heath. Limited feedback unitary precoding for spatial multiplexing systems. *IEEE Transactions on Information Theory*, 51(8):2967–2976, Aug 2005.

[57] P. Markopoulos and G. Karystinos. Noncoherent alamouti phase-shift keying with full-rate encoding and polynomial-complexity maximum-likelihood decoding. *IEEE Transactions on Wireless Communications*, 16(10):6688–6697, 2017.

[58] T. Marzetta and B. Hochwald. Capacity of a mobile multiple-antenna communication link in Rayleigh flat fading. *IEEE Transactions on Information Theory*, 45(1):139–157, January 1999.

[59] M. McCloud, M. Brehler, and M. Varanasi. Signal design and convolutional coding for noncoherent space-time communication on the block-rayleigh-fading channel. *IEEE Transactions on Information Theory*, 48(5):1186–1194, 2002.

[60] M. Médard and R. Gallager. Bandwidth scaling for fading multipath channels. *IEEE Transactions on Information Theory*, 48(4):840–852, 2002.

[61] V. Nguyen. Performance analysis of differential space–time modulation. *IEEE Transactions on Information Theory*, 58(5):2620–2632, 2012.

[62] M. Nielsen and I. Chuang. *Quantum Computation and Quantum Information*. Cambridge University Press, 2017.

[63] F. Oggier, N. Sloane, S. Diggavi, and R. Calderbank. Nonintersecting subspaces based on finite alphabets. *IEEE Transactions on Information Theory*, 51(12):4320–4325, 2005.

[64] J. Pierce. Ultimate performance of M-ary transmissions on fading channels. *IEEE Transactions on Information Theory*, 12(1):2–5, January 1966.

[65] Y. Polyanskiy, H. Poor, and S. Verdú. Channel coding rate in the finite blocklength regime. *IEEE Transactions on Information Theory*, 56(5):2307, 2010.

[66] Y. Polyanskiy and S. Verdú. Scalar coherent fading channel: Dispersion analysis. In *2011 IEEE International Symposium on Information Theory Proceedings*, pages 2959–2963. IEEE, 2011.

[67] J. Preskill. Quantum computing in the NISQ era and beyond. *Quantum*, 2:79, 2018.

[68] J. Proakis. *Digital Communications*. Electrical engineering series. McGraw-Hill, 2001.

[69] P. Pun and P. Ho. Fano multiple-symbol differential detectors for differential unitary space–time modulation. *IEEE Transactions on Communications*, 55(3):540–550, 2007.

[70] X. Qiang, X. Zhou, J. Wang, C. Wilkes, T. Loke, S. O'Gara, L. Kling, G. Marshall, R. Santagati, T. Ralph, et al. Large-scale silicon quantum

photonics implementing arbitrary two-qubit processing. *Nature Photonics*, 12(9):534, 2018.

[71] C. Rao and B. Hassibi. Analysis of multiple-antenna wireless links at low snr. *IEEE Transactions on Information Theory*, 50(9):2123–2130, 2004.

[72] M. Rasekh, Z. Marzi, Y. Zhu, U. Madhow, and H. Zheng. Noncoherent mmwave path tracking. In *Proceedings of the 18th International Workshop on Mobile Computing Systems and Applications*, pages 13–18. ACM, 2017.

[73] R. Raussendorf, D. Browne, and H. Briegel. Measurement-based quantum computation on cluster states. *Physical Review A*, 68(2):022312, 2003.

[74] R. Schober and L. Lampe. Noncoherent receivers for differential space-time modulation. *IEEE Transactions on Communications*, 50(5):768–777, 2002.

[75] P. Schulz, M. Matthe, H. Klessig, M. Simsek, G. Fettweis, J. Ansari, S. Ashraf, B. Almeroth, J. Voigt, I. Riedel, et al. Latency critical IoT applications in 5G: Perspective on the design of radio interface and network architecture. *IEEE Communications Magazine*, 55(2):70–78, 2017.

[76] V. Sethuraman, L. Wang, B. Hajek, and A. Lapidoth. Low-SNR capacity of noncoherent fading channels. *IEEE Transactions on Information Theory*, 55(4):1555–1574, 2009.

[77] S. Sheldon, L. Bishop, E. Magesan, S. Filipp, J. Chow, and J. Gambetta. Characterizing errors on qubit operations via iterative randomized benchmarking. *Physical Review A*, 93(1):012301, 2016.

[78] A. Shokrollahi, B. Hassibi, B. Hochwald, and W. Sweldens. Representation theory for high-rate multiple-antenna code design. *IEEE Transactions on Information Theory*, 47(6):2335–2367, 2001.

[79] P. Shor. Algorithms for quantum computation: Discrete logarithms and factoring. In *Proceedings 35th annual symposium on foundations of computer science*, pages 124–134. Ieee, 1994.

[80] R. Spreeuw. Classical wave-optics analogy of quantum-information processing. *Physical Review A*, 63(6):062302, 2001.

[81] S. Srinivasan and M. Varanasi. Code design for the low SNR noncoherent MIMO block rayleigh fading channel. In *Proceedings of the International Symposium on Information Theory, 2005.*, pages 2218–2222. IEEE, 2005.

[82] S. Srinivasan and M. Varanasi. Optimal constellations for the low-SNR noncoherent MIMO block rayleigh-fading channel. *IEEE Transactions on Information Theory*, 55(2):776–796, 2009.

[83] T. Strohmer and R. Heath Jr. Grassmannian frames with applications to coding and communication. *Applied and Computational Harmonic Analysis*, 14(3):257–275, 2003.

[84] V. Tarokh and H. Jafarkhani. A differential detection scheme for transmit diversity. *IEEE Journal on Selected Areas in Communications*, 18(7):1169–1174, 2000.

[85] V. Tarokh and I. Kim. Existence and construction of noncoherent unitary space-time codes. *IEEE Transactions on Information Theory*, 48(12):3112–3117, 2002.

[86] I. Telatar and D. Tse. Capacity and mutual information of wideband multipath fading channels. *IEEE Transactions on Information Theory*, 46(4):1384–1400, 2000.

[87] P. Thian, Y. Pooi, and S. Chun. Bit error probability for orthogonal space time block codes with differential detection. In *The Ninth International Conference on Communications Systems, 2004*, pages 296–300, Sep. 2004.

[88] D. Torrieri, S. Cheng, and M. Valenti. Robust frequency hopping for interference and fading channels. *IEEE Transactions on Communications*, 56(8):1343–1351, 2008.

[89] V. Va, J. Choi, and R. Heath Jr. The impact of beamwidth on temporal channel variation in vehicular channels and its implications. *IEEE Transactions on Vehicular Technology*, 66(6):5014–5029, 2017.

[90] S. Verdú. Spectral efficiency in the wideband regime. *IEEE Transactions on Information Theory*, 48(6):1319–1343, 2002.

[91] D. Warrier and U. Madhow. Spectrally efficient noncoherent communication. *IEEE Transactions on Information Theory*, 48(3):651–668, 2002.

[92] X. Wu and R. Srikant. Mimo channels in the low-snr regime: Communication rate, error exponent, and signal peakiness. *IEEE Transactions on Information Theory*, 53(4):1290–1309, 2007.

[93] D. Xia, J. Zhang, S. Dumitrescu, and F. Gong. Full diversity noncoherent alamouti-based toeplitz space-time block codes. *IEEE Transactions on Signal Processing*, 60(10):5241–5253, 2012.

[94] W. Yang, G. Durisi, T. Koch, and Y. Polyanskiy. Quasi-static multiple-antenna fading channels at finite blocklength. *IEEE Transactions on Information Theory*, 60(7):4232–4265, 2014.

[95] W. Yang, G. Durisi, and E. Riegler. On the capacity of large-MIMO block-fading channels. *arXiv preprint arXiv:1202.0168*, 2012.

[96] W. Zhao, G. Leus, and G. Giannakis. Orthogonal design of unitary constellations for uncoded and trellis-coded noncoherent space-time systems. *IEEE Transactions on Information Theory*, 50(6):1319–1327, 2004.

[97] L. Zheng and D. Tse. Communication on the Grassmann manifold: A geometric approach to the noncoherent multiple-antenna channel. *IEEE Transactions on Information Theory*, 48(2):359–383, 2002.

[98] L. Zheng, D. Tse, and M. Médard. Channel coherence in the low-SNR regime. *IEEE Transactions on Information Theory*, 53(3):976–997, 2007.

[99] X. Zhu, S. Chen, H. Hu, X. Su, and Y. Shi. TDD-based mobile communication solutions for high-speed railway scenarios. *IEEE Wireless Communications*, 20(6):22–29, 2013.